# REPORT DOCUMENTATION PAGE

*Form Approved*
*OMB No. 0704-0188*

Public reporting burden for this collection of information is estimated to average 1 hour per response, including the time for reviewing instructions, searching existing data sources, gathering and maintaining the data needed, and completing and reviewing this collection of information. Send comments regarding this burden estimate or any other aspect of this collection of information, including suggestions for reducing this burden to Department of Defense, Washington Headquarters Services, Directorate for Information Operations and Reports (0704-0188), 1215 Jefferson Davis Highway, Suite 1204, Arlington, VA 22202-4302. Respondents should be aware that notwithstanding any other provision of law, no person shall be subject to any penalty for failing to comply with a collection of information if it does not display a currently valid OMB control number. **PLEASE DO NOT RETURN YOUR FORM TO THE ABOVE ADDRESS.**

**1. REPORT DATE** *(DD-MM-YYYY)*
6/6/18

**2. REPORT TYPE**
Final Technical

**3. DATES COVERED** *(From - To)*
01/01/2010 – 12/31/2014

**4. TITLE AND SUBTITLE**
Kuroshio Graduate Student Support

**5a. CONTRACT NUMBER**

**5b. GRANT NUMBER**
N00014-10-1-0311

**5c. PROGRAM ELEMENT NUMBER**

**6. AUTHOR(S)**
Craig M. Lee, Eric D'Asaro, Leah Johnson and Kai-Chieh Yang

**5d. PROJECT NUMBER**

**5e. TASK NUMBER**

**5f. WORK UNIT NUMBER**

**7. PERFORMING ORGANIZATION NAME(S) AND ADDRESS(ES)**
University of Washington – Applied Physics Laboratory, Box 355640
1013 NE 40th Street
Seattle, WA 98105-6698

**8. PERFORMING ORGANIZATION REPORT NUMBER**

**9. SPONSORING / MONITORING AGENCY NAME(S) AND ADDRESS(ES)**
Office of Naval Research
875 North Randolph Street
Arlington, VA 22203-1995

**10. SPONSOR/MONITOR'S ACRONYM(S)**
ONR

**11. SPONSOR/MONITOR'S REPORT NUMBER(S)**

**12. DISTRIBUTION / AVAILABILITY STATEMENT:**

Distribution Statement A: Approved for public release; distribution is unlimited.

**13. SUPPLEMENTARY NOTES**

**14. ABSTRACT**

This grant provided partial support for two students, Ms. Kai-Chieh Yang (M.S. 2012) and Ms. Leah Johnson (M.S. 2014, PhD. 2018). Ms. Yang assisted with ongoing glider-based observational programs in the Kuroshio Current, in the vicinity of Luzon Strait, and worked on analysis of the resulting data. Her work contributed to two papers, Rainville et al. (2013), which documented the propagation of internal tides generated at Luzon Strait, and Yang et al. (2015), which revealed the existence of a dual-core structure to the Kuroshio east of Taiwan. Ms Yang continued her studies at National Taiwan University after completion of her M.S. at the University of Washington, and received her Ph.D. in 2017. Ms. Johnson initially focused on understanding signatures in upper ocean variability that might be indicative of restratification driven by mixed layer instabilities – submesoscale eddies that can rapidly restratify the upper ocean and searched for these 'fingerprints' over the global ocean, using data set provide by the Argo program, reporting her results in Johnson et al. (2016). Her Ph.D. research investigates these and related dynamics using 3D synoptic surveys in the California Current, conducted as part of the ONR Assessing the Effects of Submesocale Ocean Parameterizations (AESOP) Departmental Research Initiative.

**15. SUBJECT TERMS**
Kuroshio Current, western boundary currents, mesoscale, submesoscale, gliders

| **16. SECURITY CLASSIFICATION OF:** | | | **17. LIMITATION OF ABSTRACT** | **18. NUMBER OF PAGES** | **19a. NAME OF RESPONSIBLE PERSON** |
|---|---|---|---|---|---|
| **a. REPORT** | **b. ABSTRACT** | **c. THIS PAGE** | | | Crag M. Lee |
| Unclassified | Unclassified | Unclassified | UU | 21 | **19b. TELEPHONE NUMBER** *(include area code)* (206) 543-1300 |

**Standard Form 298 (Rev. 8-98)**
**Prescribed by ANSI Std. Z39.18**

# Final Report: Kuroshio Graduate Student Support

Craig M. Lee
Applied Physics Laboratory, University of Washington
1013 NE 40th St.
Seattle, WA 98105-6698
phone: (206) 685-7656 fax: (206) 543-6785 email: craig@apl.washington.edu

Grant Number: N00014-10-1-0311
http://opd.apl.washington.edu/~craig

## LONG-TERM GOALS

This study contributes to long-term efforts toward understanding:

- Dynamics and variability of the Kuroshio Current.
- Circulation of the Western Pacific.
- Submesocale dynamics.

## SUMMARY

This grant provided partial support for two students, Ms. Kai-Chieh Yang (M.S. 2012) and Ms. Leah Johnson (M.S. 2014, PhD. 2018).

Ms. Yang assisted with ongoing glider-based observational programs in the Kuroshio Current, in the vicinity of Luzon Strait, and worked on analysis of the resulting data. Her work contributed to two papers, Rainville et al. (2013), which documented the propagation of internal tides generated at Luzon Strait, and Yang et al. (2015), which investigated Kuroshio structure east of Taiwan. Ms Yang continued her studies at National Taiwan University after completion of her M.S. at the University of Washington, and received her Ph.D. in 2017.

Ms. Johnson initially focused on understanding signatures in upper ocean variability that might be indicative of restratification driven by mixed layer instabilities – submesoscale eddies that can rapidly restratify the upper ocean. She then searched for these 'fingerprints' over the global ocean, using data set provide by the Argo program, reporting her results in Johnson et al. (2016). Her Ph.D. research investigates these and related dynamics using 3D synoptic surveys in the California Current, conducted as part of the ONR Assessing the Effects of Submesocale Ocean Parameterizations (AESOP) Departmental Research Initiative.

Scientific findings resulting from this grant are best described in three publications listed in the references, and also appended to this report.

**PUBLICATIONS**

Johnson, L., C.M. Lee and E.A. D'Asaro, 2016: Observational Evidence of Lateral Slumping Induced Springtime Stratification. *Journal of Physical Oceanography*. doi:10.1175/JPO-D-15-0163.1.

Rainville, L., C. M. Lee, D. L. Rudnick, and K.-C. Yang, 2013: Propagation of internal tides generated near Luzon Strait: Observations from autonomous gliders. *Journal of Geophysical Research*, 118, doi:10.1002/jgrc.20293.

Yang, K.-C., J. Wang, C.M. Lee, B. Ma, R.-C. Lien, S. Jan, Y.J. Yang, and M.-H. Chang. 2015. Two mechanisms cause dual velocity maxima in the Kuroshio east of Taiwan. *Oceanography* 28(4):64–73, https://doi.org/10.5670/oceanog.2015.82.

# Global Estimates of Lateral Springtime Restratification

LEAH JOHNSON, CRAIG M. LEE, AND ERIC A. D'ASARO

*Applied Physics Laboratory, University of Washington, Seattle, Washington*

(Manuscript received 26 August 2015, in final form 5 February 2016)

ABSTRACT

Submesoscale frontal dynamics are thought to be of leading-order importance for stratifying the upper ocean by slumping horizontal density gradients to produce vertical stratification. Presented here is an investigation of submesoscale instabilities in the mixed layer—mixed layer eddies (MLEs)—as a potential mechanism of frontal slumping that stratifies the upper ocean during the transition from winter to spring, when wintertime forcings weaken but prior to the onset of net solar warming. Observations from the global Argo float program are compared to predictions from a one-dimensional mixed layer model to assess where in the world's oceans lateral processes influence mixed layer evolution. The model underestimates spring stratification for ~75% ± 25% of the world's oceans. Relationships between vertical and horizontal temperature and salinity gradients are used to suggest that in 30% ± 20% of the oceans this excess stratification can be attributed to the slumping of horizontal density fronts. Finally, 60% ± 10% of the frontal enhanced stratification is consistent with MLE theory, suggesting that MLEs may be responsible for enhanced stratification in 25% ± 15% of the world's oceans. Enhanced stratification from frontal tilting occurs in regions of strong horizontal density gradients (e.g., midlatitude subtropical gyres), with a small fraction occurring in regions of deep mixed layers (e.g., high latitudes). Stratification driven by MLEs appears to constrain the coexistence of sharp lateral gradients and deep wintertime mixed layers, limiting mixed layer depths in regions of large lateral density gradients, with an estimated wintertime restratification flux of order 100 W m$^{-2}$.

## 1. Introduction

The mixed layer (ML) of the upper ocean evolves in response to momentum input from winds and buoyancy fluxes (e.g., surface heat flux, inputs of freshwater and salt). Wintertime cooling and strong winds at the ocean surface drive convective overturning and mixing that homogenize the upper ocean, producing deep MLs. During the transition into spring, warmer, more buoyant waters cap the underlying wintertime ML, inhibiting deep mixing and stratifying the upper ocean. This springtime stratification has large impacts on upper-ocean biogeochemistry (Sverdrup 1953), air–sea heat and gas exchange (Belcher et al. 2012), and water mass formation (Worthington 1953). One-dimensional dynamics describe springtime mixed layer evolution as a competition between deepening by convective overturning and wind mixing and shoaling due to buoyancy input from increased solar warming (Figs. 1a,b). The ML shallows as increasing net surface heat flux overcomes mixing and convection. This one-dimensional view, however, neglects lateral processes that can advect buoyancy and alter the stratification of the upper ocean.

Large-scale lateral density gradients within the ML are the net product of numerous, smaller, sharper gradients and fronts. Consider just one of these sharp fronts (Fig. 1a); the upper ML is vertically homogenous, but the lateral structure reveals a sharp density difference. Slumping this small front transforms the horizontal density gradient into a vertical stratification (Fig. 1c). This transformation rearranges the lateral density structure, suggesting that initial temperature–salinity (TS) horizontal gradients eventually constitute the vertical stratification. One small front stratifies the upper ocean locally, and a field of tilting fronts creates a large-scale stratification.

Recent work suggests that dynamics associated with submesoscale $O$(10–100) km fronts are a leading-order contributor of upper-ocean stratification in the absence of solar warming. (Boccaletti et al. 2007; Thomas et al. 2008). During wintertime, surface cooling and wind-driven turbulent mixing act to keep the upper-ocean vertically

*Corresponding author address*: Leah Johnson, Applied Physics Laboratory, University of Washington, 1013 NE 40th Street, Seattle, WA 98105.
E-mail: leahj@apl.washington.edu

DOI: 10.1175/JPO-D-15-0163.1

© 2016 American Meteorological Society

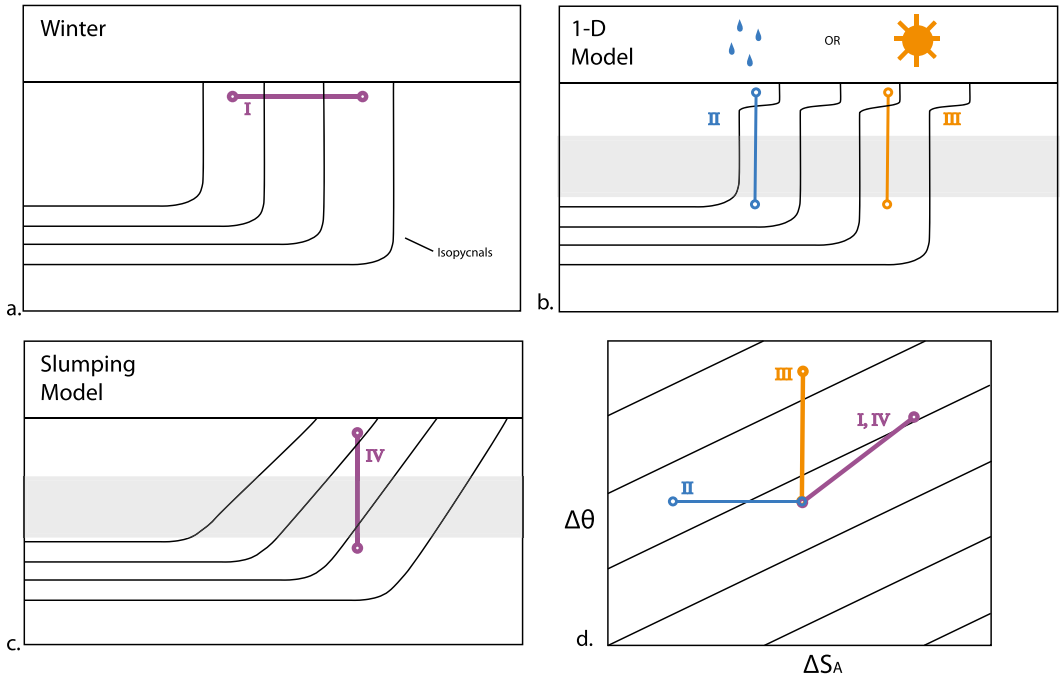


FIG. 1. (a) Schematic of a mixed layer density front during winter. Surface winds and deep convection keep the upper-ocean vertically homogenous, yet lateral changes in buoyancy are retained. Horizontal changes in buoyancy comprise gradients of temperature and salinity (I). (b) One-dimensional model. During spring, the upper ocean stratifies as a result of freshwater input (II) and solar warming (III) at the ocean surface. (c) Slumping model. Stratification at a front can occur without buoyancy input at the surface. As surface forcing weakens, the nearly vertical isopycnals in (a) begin to tilt as light water is advected over heavy water (IV). In this scenario, the horizontal density gradient is being transformed into a vertical stratification. Horizontal TS gradients become vertical gradients. Gray shaded areas in (b) and (c) represent the 50%–90% depth range used in this analysis. (d) Gradients of TS provide insight into the mechanisms that stratify the upper ocean in the transition into spring.

homogenous in the presence of sharp horizontal density contrasts (e.g., Fig. 1a). These sharp gradients provide a source of available potential energy (APE). Dynamics that tap into this APE can result in baroclinic instabilities that grow into submesoscale eddies [ML eddies (MLEs); Boccaletti et al. 2007]. The flattening of isopycnals by MLEs is inhibited by wintertime wind mixing and cooling that work to maintain the vertical homogeneity of the ML. But theory and model simulations predict that frontal slumping has an important role in spring, when forcing by winds and surface cooling weaken but before net solar warming dominates the vertical buoyancy of the upper ocean. MLEs could explain why one-dimensional mixed layer models fail to describe springtime upper-ocean restratification accurately. (Boccaletti et al. 2007; Thomas and Ferrari 2008; Fox-Kemper et al. 2008; Mahadevan et al. 2010).

This paper focuses on MLEs as the source of springtime restratification, yet there are other leading-order frontal processes that modify stratification in the ML. In the absence of forcing, vertical isopycnals of a front will undergo geostrophic adjustment and tilt to a resting state, as described by Tandon and Garrett (1994). Frontogenetic flows induce ageostrophic secondary circulations that flatten isopycnals (Hoskins and Bretherton 1972). Additionally, frictional effects are shown to be as influential as MLEs at modulating ML stratification. Winds blowing up/downfront have restratifying/destratifying effects on the upper ocean (Thomas and Lee 2005; Mahadevan et al. 2010).

This work takes a global approach to investigate the following: Why do one-dimensional mixed layer models fail to replicate ML evolution during the transition from winter to spring (section 2)? Can the observed stratification in excess of model predictions be attributed to lateral slumping of submesoscale fronts (section 3)? Does MLE theory explain patterns of stratification induced by lateral slumping (section 4)? After a regional discussion of the global results (section 5), alternate frontal processes that modify ML stratification are explored (section 6).

### *a. Stratification by one-dimensional processes*

ML evolution has been described using one-dimensional dynamics (e.g., Kraus and Turner 1967; Price et al. 1986;

Large et al. 1994), balancing deepening by wind mixing and convective overturning against shallowing by surface warming and freshwater input. Global simulations that use these parameterizations overestimate ML depth (Fox-Kemper et al. 2011). This study employs a one-dimensional model [Price–Weller–Pinkel (PWP)] to simulate upper-ocean response to surface heat flux, winds stress, and freshwater input (Price et al. 1986). Modeled vertical structure is compared with upper-ocean observations collected by the global Argo program (Roemmich et al. 2009) to assess where the spring transition cannot be explained by one-dimensional processes and pinpoint regions where lateral processes are likely influential. Section 2a provides details about the 1D model and data processing.

### b. Stratification by lateral slumping

Adiabatic slumping of a front ultimately results in an upward transport of buoyancy as the lateral density gradients (e.g., Fig. 1a) are transformed into a vertical stratification (e.g., Fig. 1c). The rearrangements of isopycnals imply that lateral gradients of TS are rotated into vertical gradients. This relationship between vertical and horizontal TS will be used to isolate regions where adiabatic frontal tilting could account for the shortfall of PWP model simulations compared to Argo float observations and is discussed in section 3.

### c. Lateral slumping by mixed layer eddies

Boccaletti et al. (2007) and Fox-Kemper et al. (2008) propose that lateral slumping, and the resulting stratification of the ML, occurs via MLEs. As wintertime forcing weakens, vertical isopycnals begin to undergo adjustment. Direct slumping due to geostrophic adjustment results in a modest increase in ML stratification as isopycnals oscillate around a mean state (Tandon and Garrett 1994). However, at submesoscale fronts, the Rossby number approaches $O(1)$ and geostrophy breaks down, allowing these oscillations (or other perturbations) to grow into baroclinic instabilities that develop MLEs (Boccaletti et al. 2007). These submesoscale instabilities draw upon the APE of the lateral density gradients, resulting in an eddy overturning circulation with large vertical velocities that redistribute density and flatten the initially nearly vertical isopycnals (Boccaletti et al. 2007; Fox-Kemper et al. 2008). The existence of submesoscale fronts during winter suggests that fields of MLEs could have an impact on large-scale stratification that is not captured by one-dimensional parameterizations of the upper ocean. Upper-ocean buoyancy transport by the MLE overturning circulation competes with convection and wind mixing that act to destroy vertical stratification (Mahadevan et al. 2010).

Fox-Kemper et al. (2008) propose a parameterization for the slumping of a single submesoscale front into vertical stratification by a MLE. The overturning streamfunction is

$$\Psi_o = C_e \frac{\nabla b H^2}{|f|} \mu(z), \quad \text{and} \tag{1}$$

$$\mu(z) = \left[1 - \left(\frac{2z}{H} + 1\right)^2\right]\left[1 + \frac{5}{21}\left(\frac{2z}{H} + 1\right)^2\right], \tag{2}$$

where $b = -g(\rho/\rho_o)$ is the buoyancy, $H$ is the ML depth, $f$ is the Coriolis parameter, and $C_e$ is 0.06–0.08.

The net effect is the transformation of horizontal density gradients into vertical stratification by an MLE; this process is potentially important for the ML buoyancy budget. Although MLEs are not a source of buoyancy, it is possible to express the overturning streamfunction $\Psi_o$ in terms of an equivalent surface heat flux (Fox-Kemper et al. 2008; Mahadevan et al. 2012):

$$Q_{\mathrm{MLE}} = \frac{c_p \rho}{g \alpha_T} \frac{C_e |\nabla b|^2 H^2}{|f|}, \tag{3}$$

where $c_p$ is the specific heat capacity of water, and $\alpha_T$ is the thermal expansion coefficient.

Here, the stratifying effect of an MLE is stated as a surface heat flux equivalent $Q_{\mathrm{MLE}}$. This facilitates comparison with air–sea heat fluxes and formulates the impact of this three-dimensional process in a one-dimensional framework.

This parameterization [(1)] is designed for a single, resolved submesoscale front and is thus insufficient for larger-scale models. The resolution of global simulations [$O(100)$ km] cannot resolve the submesoscale lateral density gradients [$O(1–10)$ km]. Modeled gradients (and observed large-scale gradients) must thus be scaled appropriately for use in the Fox-Kemper parameterization [(1)]. Observational studies show that power spectra fall off at about $k^{-2}$ for horizontal variance of velocity and tracers (Capet et al. 2008) and potential density. Fox-Kemper et al. (2011) assume this and derived a relationship between large-scale density structure and small-scale gradients. This relationship extends the utility of (1) to coarser-scale models through a scale factor $\Delta s/L_f$ (Fox-Kemper et al. 2011), where $\Delta$ is the grid resolution and $L_f$ is a typical width of a submesoscale front taken to be the maximum of three possible estimates:

$$L_f = \max\left(\frac{NH}{|f|}, \frac{\nabla b H}{f^2}, L_{f\min}\right). \tag{4}$$

The first estimate suggests that frontal width scales as the ML deformation radius (Hosegood et al. 2006). The second assumes that stratification in the ML before a MLE is a result of Rossby adjustment, which scales as $N^2f^2 = \nabla b^2$ (Tandon and Garrett 1994). The third estimate $L_{f\min}$ is a tuned parameter for frontal width approximated to be 0.2–5 km (Fox-Kemper et al. 2011).

In global simulations, the scaling factor is applied to the overturning streamfunction [(1)] such that $\Psi = (\Delta s/L_f)\Psi_o$. Similarly, it is applied to (3):

$$Q_{\mathrm{MLE}} = \frac{\Delta s}{L_f}\frac{c_p\rho}{g\alpha_T}\frac{C_e|\nabla b|^2H^2}{|f|}, \tag{5}$$

where $Q_{\mathrm{MLE}}$ represents the restratifying effects of MLEs and suggests MLEs will dominate upper-ocean stratification when $Q_{\mathrm{MLE}}$ is comparable in magnitude to the destratifying effects of negative surface heat flux and wind mixing. This implies that observations in regions with MLEs would experience earlier onset of stratification than predicted by one-dimensional processes (Mahadevan et al. 2012). In this study, $Q_{\mathrm{MLE}}$ is used to explore where regions of lateral slumping can be attributed to MLEs.

Parameterizations of MLE-induced stratification have been integrated into global circulation models (GCM) on top of current one-dimensional ML parameterizations [e.g., CCSM4, Danabasoglu et al. 2012; global coupled carbon–climate Earth System Model (ESM2), Dunne et al. 2012], yet no observational study has assessed whether this parameterization is appropriate throughout the world's oceans. Mahadevan et al. (2012) use data and model simulations to show that increased ML stratification in the Icelandic basin (IB) could be attributed to the influence of MLEs. Increased stratification was observed by autonomous gliders and is evident in climatological data from the region. The climatological signature of enhanced stratification, combined with the theoretical development of the MLE parameterization for GCMs, provide a large-scale fingerprint of the integrated effects of this small-scale process that could be observed on a global scale.

Here, global observations of vertical stratification and ML TS are used to identify regions of enhanced stratification produced by lateral slumping of horizontal density gradients. Results are compared with global maps of $Q_{\mathrm{MLE}}$ to assess where MLE theory can predict these patterns of observed stratification induced by lateral slumping. Similarities and discrepancies between these two distributions will be discussed in the context of other important ML processes.

## 2. Stratification: Model simulations versus observations

### a. Data processing

The one-dimensional PWP model (Price et al. 1986) predicts the time evolution of the vertical structure of temperature and salinity in the upper ocean. The model is forced with radiative (shortwave, longwave, and latent and sensible heat) and freshwater fluxes from the National Centers for Environmental Prediction–National Center for Atmospheric Research reanalysis 2 (NNR2) and winds from the cross-calibrated multiplatform (CCMP). Model runs are initialized with a single profile of in situ temperature and salinity calculated from Conservative Temperature $\theta$ and Absolute Salinity $S_{\mathrm{A}}$ provided by the Monthly Isopycnal/Mixed-Layer Ocean Climatology (MIMOC; Schmidtko et al. 2012). Each model run starts in winter, when ML depths are assumed to be deepening (1 January for the Northern Hemisphere and 1 July in the Southern Hemisphere). The model is then run for 250 days with 2-m vertical resolution and 6-h temporal resolution. Runs are performed throughout the global oceans at locations defined by NNR2 and initialized for five separate years between 2006 and 2010. This study also employs Argo float profiles from the program's global database (Roemmich et al. 2009) collected between 2002 and 2013 with a quality control flag of 2 or better. Hereinafter, analysis is conducted in terms of $\theta$ and $S_{\mathrm{A}}$ (IOC et al. 2010).

This analysis focuses on the ML evolution from winter to spring, during the period before the ocean experiences significant surface heating, when lateral processes are theorized to have a large role in governing upper-ocean stratification on time scales of days. Throughout, time is expressed relative to the day on which total radiative heat flux $Q_{\mathrm{NET}}$ changes sign from surface cooling (negative) to surface warming (positive) $t_{_\mathrm{QNET0}}$. This allows all years of model output and observations to be collapsed onto a single time axis. Quantifying $t_{_\mathrm{QNET0}}$ is complicated by fluctuations in radiative heat fluxes; sign change can be obscured by intermittent warming followed a period of cooling. Here, $t_{_\mathrm{QNET0}}$ for each year is determined by identifying the minimum of the zero-phase, low-pass (length of 20 days) filtered, time-integrated $Q_{\mathrm{NET}}$ derived from NNR2. Both the integration and low-pass filter act to smooth the data. A 20-day filter was determined through visual inspection to be the most appropriate length to capture the minimum integrated $Q_{\mathrm{NET}}$. A Monte Carlo error estimate for $t_{_\mathrm{QNET0}}$ combines uncertainties in radiative heat flux provided by NNR2 with a range of low-pass filter lengths (7–30 days). Regions most sensitive to this calculation are the lower latitudes (<20°) with a standard deviation

of 5 days; standard deviation decreases to 3 days at higher latitudes. This range of error is propagated as background noise when calculating error in subsequent analyses (sections 2c and 3c). Regions lacking a minimum in integrated $Q_{\mathrm{NET}}$ (e.g., near the equator) were omitted from analysis.

Although spring stratification results in ML shoaling, defining the ML can be challenging because small variations in ML definition can produce results that differ greatly (e.g., Sutherland et al. 2014). This study avoids this obfuscation by focusing on stratification in the upper ocean [Brunt–Väisälä frequency; $N^2 = -(g/\rho_o)(\Delta\rho/\Delta z)$]. Differences between observed and modeled $N^2$ are used to identify regions where lateral processes may be important in the upper-ocean buoyancy budget. Model simulations of MLEs show the majority of stratification occurs in the middle of the ML (Mahadevan et al. 2010; Thomas et al. 2008), as has been confirmed in observations (Mahadevan et al. 2012). Here, the aim is to capture the evolution of stratification in the vertically homogenized wintertime upper ocean during the transition into spring. Choosing a depth range of focus is region specific, with a lower bound above the pycnocline and the upper limit sufficiently below the surface to minimize small diurnal fluctuations due to heat and wind. Therefore, $N^2$ values from the model output and observations are calculated vertically using changes in density over a depth range defined by 50%–90% of the MIMOC ML for the month before $t_{_\mathrm{QNET0}}$. Upper boundaries are capped at 10 m, which encompasses ~25% of the regions analyzed. The lower boundary accounts for uncertainties in the climatologically smoothed ML depth and provides a buffer from the stratified pycnocline. Argo quality control precision thresholds for temperature and salinity are used in a Monte Carlo error estimate, resulting in $N^2$ standard deviation $O(10^{-7})\,\mathrm{s}^{-1}$. Salinity measurements from Argo profiling floats have an accuracy of 0.001 psu; therefore, both modeled and observed profiles with a change in $S_{\mathrm{A}}$ less than 0.001 psu between the top and bottom bounds of the 50%–90% ML depth range were excluded from subsequent analysis. Imposing this salinity threshold excludes profiles with very small values of $N^2$ and therefore limits the analysis to regions that exhibit stratification $> O(10^{-7})\,\mathrm{s}^{-2}$, approximately the magnitude of error expected from Argo profile data.

### b. Case studies

Previous studies used one-dimensional mixed layer parameterizations to describe ML evolution near Ocean Weather Station Papa (OWS-P; Gill and Niller 1973; Large et al. 1994; Emerson and Stump 2010). There is good agreement between OWS-P mean observed (2002–13) and modeled (2006–10) lower ML $N^2$ as a function of $t_{_\mathrm{QNET0}}$ (Fig. 2a), suggesting that one-dimensional dynamics are sufficient to describe the evolution of upper-ocean stratification during the transition to spring, including the period prior to the onset of net surface warming.

In the wintertime IB, however, modeled $N^2$ underestimates consistently the observed $N^2$ (Fig. 2b), supporting the hypothesis that MLEs generate sporadic stratification throughout winter. Additionally, the observed $N^2$ increases before $t_{_\mathrm{QNET0}}$, consistent with the results reported by Mahadevan et al. (2012).

### c. Global studies

An analysis of the world's ocean follows a similar approach. Observed and modeled vertical profile data are binned spatially at $2 \times 2$ NNR2 data points, yielding grid resolution of 3.75° longitude and 3.78°–3.81° latitude. Within each bin, depth-averaged $N^2$ for 40–10 days before $t_{_\mathrm{QNET0}}$ (total of 30 days) are used to create a nonparameterized probability density function (PDF; i.e., kernel distribution) that provides the mode of the $N^2$ distribution. The 10-day shift away from $t_{_\mathrm{QNET0}} = 0$ accounts for uncertainties in $t_{_\mathrm{QNET0}}$ to ensure that the 1-month window excludes the period after the net surface heat flux changes to warming. The mode provides a more robust representation of the stratification in a given region by minimizing the influence of spurious events and, in general, results in lower values of observed $N^2$ than mean or median-based calculations. Regions where less than 10 ARGO profiles were available for the PDF were omitted from this analysis. Modeled and observed stratification are compared as a ratio of the two mode values ($R_{N2}$):

$$R_{N2} = \frac{N^2_{\mathrm{obs}}}{N^2_{\mathrm{mod}}}, \tag{6}$$

where an $R_{N2} > 1$ implies a larger observed stratification than what is predicted by the 1D model. Global maps of $R_{N2}$ identify regions where springtime stratification exceeds that predicted by the 1D model (Fig. 3a, orange highlights). The $R_{N2}$ error is estimated using a Monte Carlo approach, adding noise to $t_{_\mathrm{QNET0}}$, $\theta$, and $S_{\mathrm{A}}$ for repeated calculations of mode $N^2$ (Fig. 3b) Following Hosegood et al. (2006), the increase in stratification due to lateral slumping in relation to that expected from one-dimensional dynamics is $R_{N2} \approx 1.5$. Adopting this as a threshold yields an estimate that one-dimensional dynamics fail to reproduce observed springtime stratification in 75% ± 25% of the oceans analyzed in this study, where error is estimated using values shown in Fig. 3b. A more conservative threshold of $R_{N2} > 2$ suggests that 60% ± 25% of observed springtime stratification cannot be explained by one-dimensional dynamics.

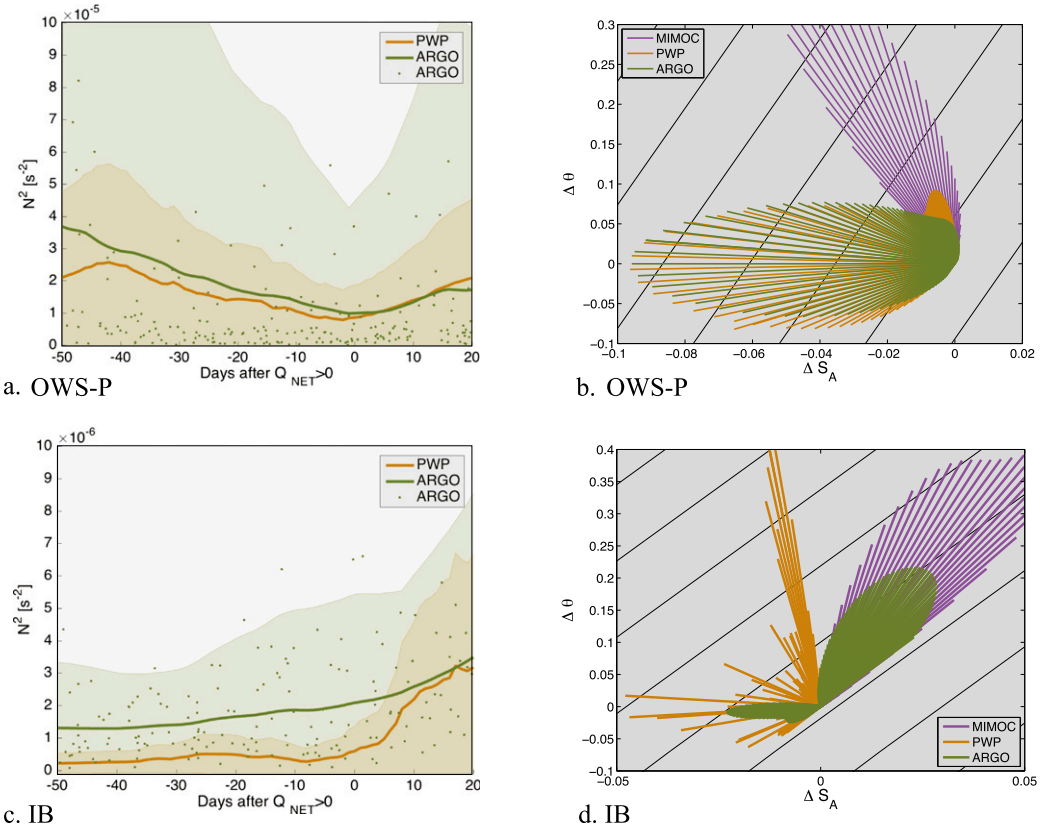


FIG. 2. (a) Mean stratification at Ocean Weather Station Papa (48°–52°N, 147°–143°W) in 50%–90% of the ML from model simulations (2006–10) and float observations (2002–13). Data were normalized to $t_{_\mathrm{QNET0}}$ for each year, then 15-day means (lines) were plotted along with 2 × std dev (shaded) for observations (green) and model (orange). Individual data points from observations are plotted as dots (green). (b) PDF of Turner angle at Ocean Weather Station Papa projected onto $\theta$–$S_\mathrm{A}$ space. For each vector, the angle is determined using (7) and (8) for model (orange), observations (green), and horizontal (purple). The length of each line is weighted to the magnitude of the PDF for the Turner angle. Here, observations match the 1D model as in Figs. 1b and 1d. (c) As in (a), but for the Icelandic basin 58°–62°N, 24°–20°W. (d) As in (b), but for the Icelandic basin. Here, observations match the horizontal density gradient model as in Figs. 1c and 1d.

## 3. Signatures of isopycnal tilting

### a. Data analysis

Adiabatic slumping of density fronts produces vertical stratification with a TS structure similar to that of the horizontal density gradient (e.g., Fig. 1). Therefore TS relationships will be used to isolate regions where excess stratification may result from tilted horizontal density gradients from regions where other processes are at work. A Turner angle provides a metric to quantify the relative contributions of temperature and salinity to density. Turner angles for horizontal $\mathrm{Tu}_H$ and vertical $\mathrm{Tu}_V$ gradients are defined as

$$\mathrm{Tu}_V = \tan^{-1}\left(\alpha\frac{\partial\theta}{\partial z} - \beta\frac{\partial S_\mathrm{A}}{\partial z}, \alpha\frac{\partial\theta}{\partial z} + \beta\frac{\partial S_\mathrm{A}}{\partial z}\right), \quad \text{and} \tag{7}$$

$$\mathrm{Tu}_H = \tan^{-1}(\alpha\partial\theta - \beta\partial S_\mathrm{A}, \alpha\partial\theta + \beta\partial S_\mathrm{A}), \tag{8}$$

where $\partial$ is the difference between data points calculated across isopycnals, and $\alpha$ and $\beta$ are the thermal expansion and saline contraction coefficients, respectively. The term $\mathrm{Tu}_V$ is determined for each Argo profile using (7) by taking data points of $\theta$ and $S_\mathrm{A}$ at the upper and lower bounds of the 50%–90% ML depth range. The gradient $\mathrm{Tu}_H$ is calculated using monthly MIMOC fields for each 0.5° grid point by fitting a plane to the surface density values at eight neighboring grid points. Surface $\theta$ and $S_\mathrm{A}$ along the inclination of the fitted plane (i.e., across gradient) were used to calculate $\mathrm{Tu}_H$ using (8).

### b. Case studies

Turner angles support the inferences drawn from the comparison of one-dimensional simulations and float observations at OWS-P and the IB. To examine the relationship between $\theta$ and $S_\mathrm{A}$ 40–10 days before the heat flux changes sign, PDFs of the Turner angle $\mathrm{Tu}_V$ are projected

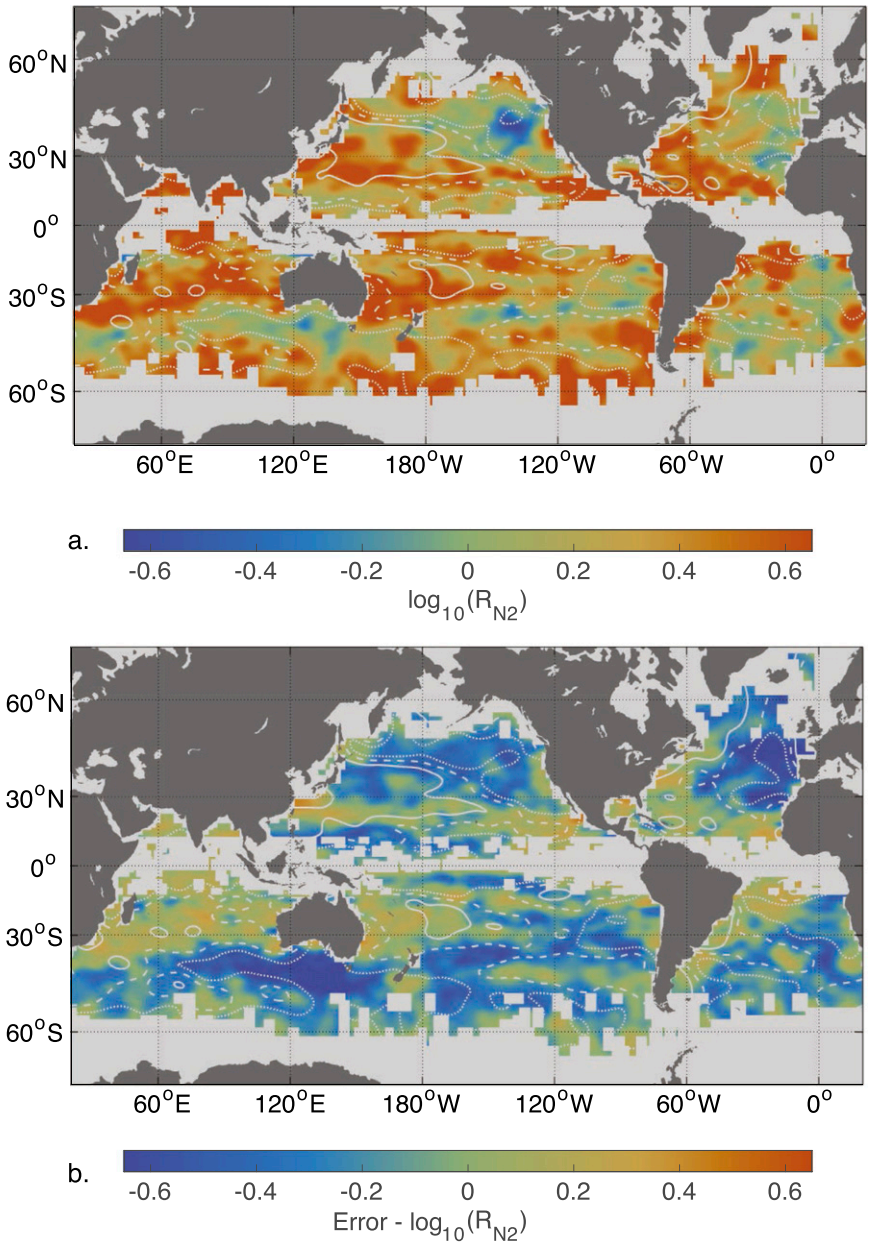


FIG. 3. (a) Ratio of observed stratification from Argo floats to modeled stratification using PWP ($R_{N2}$) for the month before $t_{_\mathrm{QNET0}} > 0$. (b) Error in $R_{N2}$. Contours of $Q_{\mathrm{MLE}}$ at 65 (solid), 35 (dashed), and 20 W m$^{-2}$ (dotted).

onto $\theta$–$S_{\mathrm{A}}$ space with vector magnitudes normalized to the PDF maximum. At OWS-P (Fig. 2c), vectors of observed (green) and modeled (orange) $\theta$–$S_{\mathrm{A}}$ lie atop each other, indicating that the model captures both the observed stratification and the observed $\theta$–$S_{\mathrm{A}}$ structure. Neither observed nor modeled $\mathrm{Tu}_V$ exhibits any relationship to $\mathrm{Tu}_H$ of the surrounding horizontal density structure (purple), suggesting that lateral effects have no significant role.

In the IB, however, the model's inability to replicate observed $\mathrm{Tu}_V$ (Fig. 2d) corroborates the disagreement between modeled and observed stratification. Instead, observed $\mathrm{Tu}_V$ agrees with horizontal across-isopycnal $\mathrm{Tu}_H$, indicative of the horizontal density gradients slumping to produce vertical stratification.

### c. Global studies

Monthly values of $\mathrm{Tu}_H$ were binned as in section 2c to estimate the TS structure of horizontal density gradients that would tilt to produce vertical stratification. MIMOC-derived $\mathrm{Tu}_H$ 1 month before $t_{_\mathrm{QNET0}}$

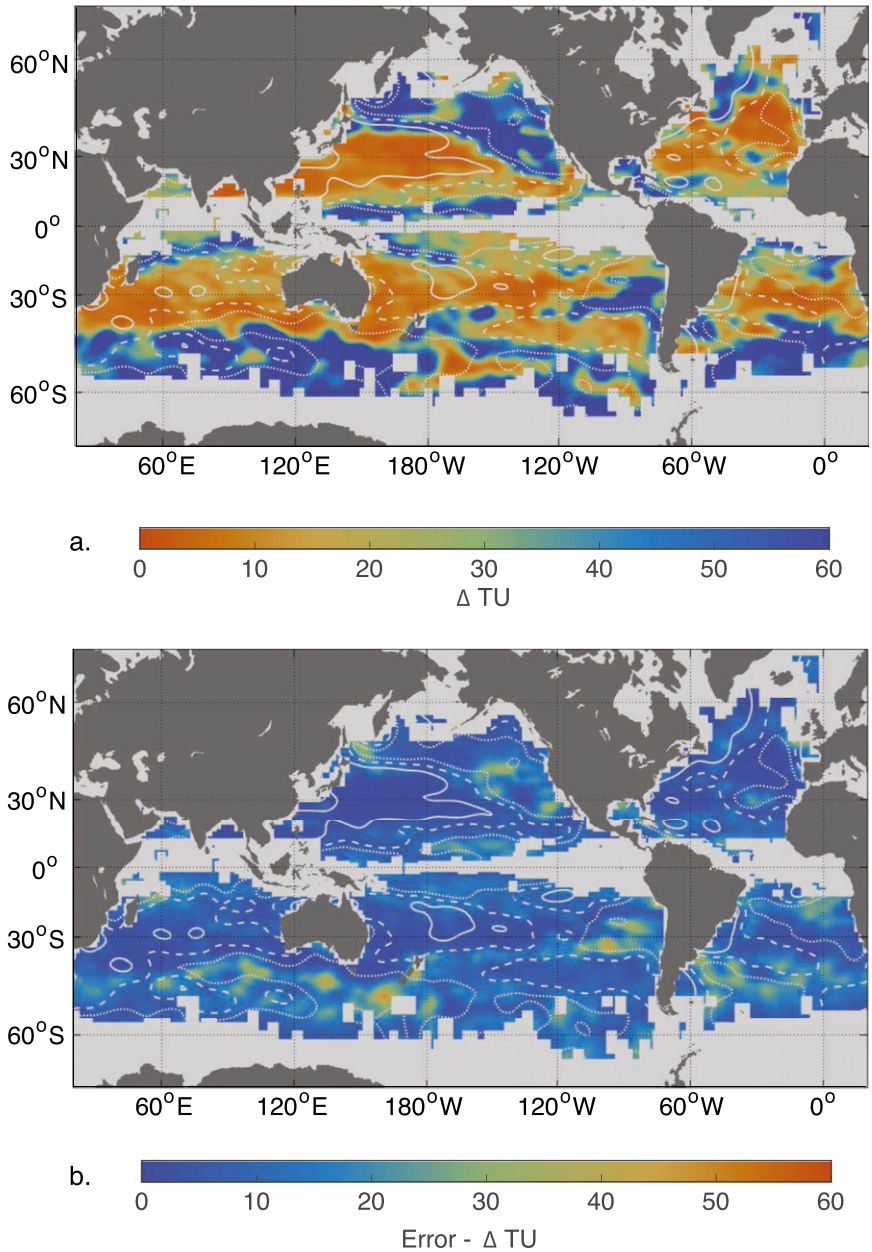


FIG. 4. (a) The ΔTu determined as $|\mathrm{Tu}_H - \mathrm{Tu}_V|$ for the month before $t_{_\mathrm{QNET0}} > 0$; $\mathrm{Tu}_H$ is derived from MIMOC and $\mathrm{Tu}_V$ from Argo data using (7) and (8). (b) Error in ΔTu. Contours of $Q_{\mathrm{MLE}}$ at 65 (solid), 35 (dashed), and 20 W m$^{-2}$ (dotted). Note the change in color bar. In (a), orange represents low values to indicate observed Tu is similar to that of the horizontal gradient. In (b), the color bar is inverted to highlight regions with large error.

were compared with $\mathrm{Tu}_V$ calculated from Argo profiles 40–10 days before $t_{_\mathrm{QNET0}}$. Differences in horizontal surface and vertical lower ML Turner angle ($\Delta\mathrm{Tu} = |\mathrm{Tu}_H - \mathrm{Tu}_V|$) are plotted in Fig. 4a. Orange regions have TS structure in the stratifying ML consistent with horizontal density gradients (i.e., similar values of $\mathrm{Tu}_H$ and $\mathrm{Tu}_V$). Note that the 10-day offset between the selected temporal ranges for $\mathrm{Tu}_H$ and $\mathrm{Tu}_V$ calculations may result in some Argo data being drawn from a different month than used to calculate $\mathrm{Tu}_H$. While $\mathrm{Tu}_H$ fluctuates interseasonally (Johnson et al. 2012), monthly changes in $\mathrm{Tu}_H$ are relatively small (<15°) in most ocean basins, with large monthly changes in $\mathrm{Tu}_H$ occurring in the low latitudes (<20°), coastal regions, and near western

boundary currents. Again, the error for ΔTu is estimated with a Monte Carlo approach by adding noise to $t_{_\mathrm{QNET0}}$, $\theta$, and $S_\mathrm{A}$ for repeated calculations of mode Tu (Fig. 4b). Of the ~75% of the oceans with $R_{N2} > 1.5$, 40% ± 25% have ΔTu < 15. Adopting these thresholds for $R_{N2}$ and ΔTu suggests that ~30% ± 20% of the oceans analyzed in this study exhibit springtime stratification influenced by the slumping of lateral density gradients.

## 4. Stratification from MLEs

### a. Global pattern of $Q_{MLE}$ versus lateral slumping-induced stratification

Maps of $Q_\mathrm{MLE}$ are created using climatological $\theta$, $S_\mathrm{A}$, and ML depth provided by MIMOC (Figs. 4a,b). The 0.5° resolution of MIMOC necessitates a scale factor, similar to what would be applied for coarse resolution models [(5)]. The terms $c_p$, $\rho$, and $\alpha$ are calculated for each MIMOC grid point, and $|\nabla b|^2$ is calculated (Fig. 4c) for each grid point using neighboring values of $\rho$ in both latitude and longitude to determine the horizontal density gradient:

$$|\nabla b| = \frac{-g}{\rho_o}(\rho_x^2 + \rho_y^2)^{1/2}. \tag{9}$$

The width $L_f$ is calculated using (4), where $N$ are mode values calculated in section 2c, and $L_{f\mathrm{min}} = 1$ km. Regions of high $Q_\mathrm{MLE}$ (Fig. 4a; orange) are associated with both the strong lateral gradients of the subtropics and the edges of the deep ML regions of the North Atlantic (NA) and the Antarctic Circumpolar Current (ACC).

The metric used to compare signatures of $R_{N2}$ and ΔTu (i.e., where enhanced stratification may result from tilting isopycnals) with $Q_\mathrm{MLE}$ is

$$\text{Weighted } \Delta\mathrm{Tu} = \frac{1}{1+\Delta\mathrm{Tu}}, \quad \text{and} \tag{10}$$

$$\text{Weighted } R_{N2} = \begin{cases} \text{for} \quad R_{N2} > 1 & 1 - \dfrac{1}{R_{N2}} \\ \text{for} \quad R_{N2} \le 1 & 0 \end{cases}. \tag{11}$$

For both, values closer to one indicate properties consistent with MLE-induced stratification (e.g., high $R_{N2}$ and ΔTu near 0). Multiplying these weighted values,

$$W_\mathrm{NT} = \text{Weighted } \Delta\mathrm{Tu} \times \text{Weighted } R_{N2}, \tag{12}$$

provides a single metric that describes where frontal slumping is likely responsible for excess upper-ocean stratification (Fig. 6a). Error for $W_\mathrm{NT}$ (Fig. 6b) is estimated by propagating error for $R_{N2}$ and ΔTu (Figs. 3b, 4b).

The subtropical North and South Pacific, the subtropical southern Indian Ocean, and the eastern South Pacific exhibit high $W_\mathrm{NT}$ coincident with high $Q_\mathrm{MLE}$ (Figs. 6, 5a). This relationship is not as discernable in the North and South Atlantic. Further discussions of these patterns are found in sections 5 and 6.

### b. Global distributions

PDFs of $H$, $\nabla b$, and $Q_\mathrm{MLE}$ (Fig. 7) describe the characteristics of high $W_\mathrm{NT}$ regions. PDFs of $Q_\mathrm{MLE}$ (Fig. 7c) for various thresholds of $W_\mathrm{NT}$ show that regions that exhibit lateral slumping-induced stratification also tend toward higher values of $Q_\mathrm{MLE}$. This reflects similarities in geographical patterns between $Q_\mathrm{MLE}$ and $W_\mathrm{NT}$ (Figs. 5a, 6) and suggests that regions of lateral slumping occur where theory predicts MLEs to be prevalent in stratifying the ML. Of regions with a $W_\mathrm{NT} > 0.5$, 60% ± 10% are also regions where $Q_\mathrm{MLE} > 40\,\mathrm{W\,m^{-2}}$ (i.e., the mode of the $Q_\mathrm{MLE}$ PDF for $W_\mathrm{NT} > 0.5$; Fig. 7a), suggesting that MLEs may be responsible for enhanced stratification in 25% ± 15% of the world's oceans.

The heat flux $Q_\mathrm{MLE}$ is proportional to $H^2$ and $\nabla b^2$, suggesting that MLEs tend to occur in regions of deep MLs and strong lateral gradients. In regions of high $W_\mathrm{NT}$, the mode of $\nabla b$ shifts toward higher values, yet the mode of H does not change. In fact, the distribution of $H$ shifts away from the deepest ML and retains only a small portion of regions with MLD greater than 200 m. The shift in $\nabla b$ is intuitive; regions of strong lateral density gradients are theorized to have an abundance of submesoscale fronts to source the APE that allows MLEs to grow, slump vertical isopycnals, and stratify the upper ocean. A more subtle mechanism sets the PDF of $H$. These results suggest that the restratifying effects of lateral slumping by MLE limit the coexistence of strong lateral density gradients and deep MLs. The shift in PDFs of $\nabla b$ and $H$ are consistent with signatures of high $W_\mathrm{NT}$ and high $Q_\mathrm{MLE}$ in the midlatitude regions of strong lateral density gradients that generally have shallower wintertime MLs. There is only a small signature of high $W_\mathrm{NT}$ and high $Q_\mathrm{MLE}$ in the high-latitude regions of modest lateral density gradients and deep MLs. This may suggest that MLEs are acting to preferentially stratify deep MLs.

### c. Horizontal buoyancy gradients versus mixed layer depths

The definition of $Q_\mathrm{MLE}$ [(3)] implies that regions with strong horizontal density contrasts and deep MLs restratify due to differential lateral advection of buoyancy, thereby reducing the ML depth and the horizontal gradient. Regions with these conditions should be unstable and rare. This relationship manifests as a negative

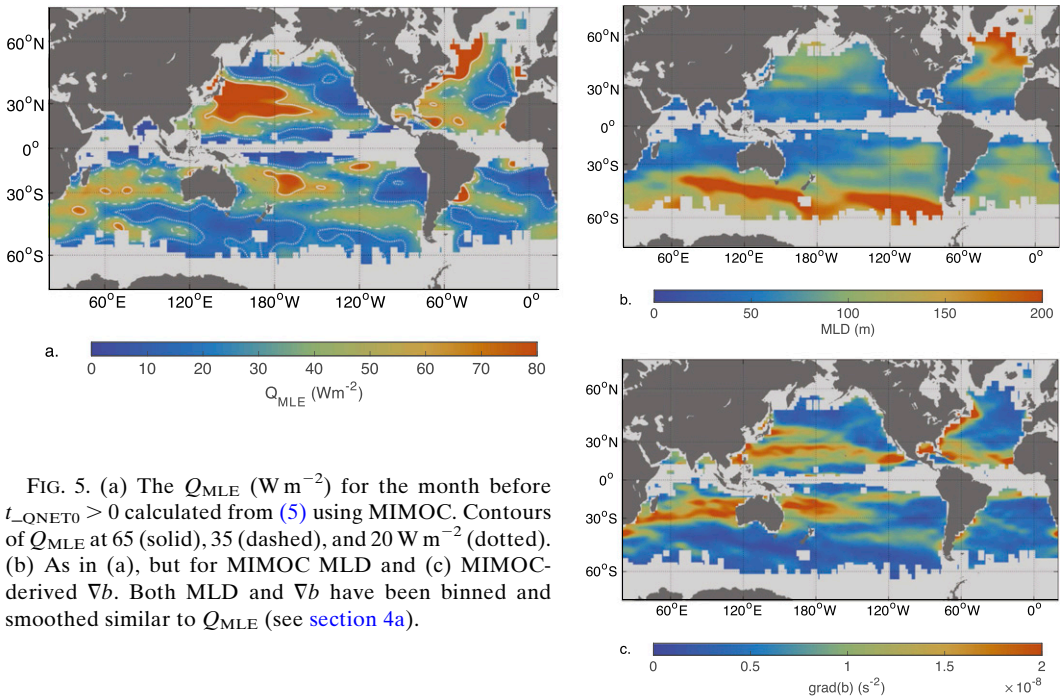


FIG. 5. (a) The $Q_{\mathrm{MLE}}$ (W m$^{-2}$) for the month before $t_{_\mathrm{QNET0}} > 0$ calculated from (5) using MIMOC. Contours of $Q_{\mathrm{MLE}}$ at 65 (solid), 35 (dashed), and 20 W m$^{-2}$ (dotted). (b) As in (a), but for MIMOC MLD and (c) MIMOC-derived $\nabla b$. Both MLD and $\nabla b$ have been binned and smoothed similar to $Q_{\mathrm{MLE}}$ (see section 4a).

correlation ($\sim -0.6$) between $H$ and $\nabla b$ in the midlatitudes (Fig. 8) and is visually apparent by comparing maps of wintertime $H$ and $\nabla b$ (Figs. 5b,c). Climatological relationships between $H$ and $\nabla b$ during winter and summer provide additional evidence (Fig. 9). Summer ML depths are generally shallow despite the magnitude of lateral buoyancy gradients, pointing to the importance of surface heating in setting stratification and ML depth (Figs. 9a,c) during this time. Wintertime surface forcing drives deep MLs (Figs. 9b,d), yet $\nabla b$ appears to set an upper bound on mixed layer depth. The slope of this relationship corresponds to a $Q_{\mathrm{MLE}}$ $O(100)$ W m$^{-2}$ (Fig. 9), comparable to values inferred by Mahadevan et al. (2012). This wintertime relationship between $H$ and $\nabla b$ is consistent with the idea that the maximum winter ML depth is set by a competition between processes that deepen the ML (e.g., wind and convective mixing) and MLEs that shallow it (Fox-Kemper and Ferrari 2008; Mahadevan et al. 2012).

## 5. Regional studies

The quantities $W_{\mathrm{NT}}$, $Q_{\mathrm{MLE}}$, $R_{N2}$, and $\Delta$Tu exhibit latitudinal-dependent correlations (Fig. 10) that provide a framework for closer examination of regional patterns of MLE influence. Correlations between $W_{\mathrm{NT}}$ and $Q_{\mathrm{MLE}}$ are largest at midlatitudes and drop off near the equator and higher latitudes, with a small increase in the high-latitude Southern Ocean. This discussion considers the results of Figs. 3, 4, 7, and 8 in the context of $Q_{\mathrm{MLE}}$ (Fig. 5).

### a. Midlatitude

High $W_{\mathrm{NT}}$ coincides with high $Q_{\mathrm{MLE}}$ in regions associated with subtropical gyres and convergent flows throughout most ocean basins. This geographic distribution is consistent with PDF shifts (Fig. 7) that suggest the majority of lateral slumping is occurring in regions with strong gradients and shallower MLs and can be seen in the midlatitude correlation between $W_{\mathrm{NT}}$ and $Q_{\mathrm{MLE}}$ (Fig. 8). The band of $W_{\mathrm{NT}}$ extending from Japan to Mexico coincides with the sharp gradients of the North Pacific convergence zone and subtropical front (Fig. 5c). Wintertime observations from this region (Hosegood et al. 2006, 2013; Shcherbina et al. 2009) reveal submesoscale dynamics of lateral slumping and possible ML and symmetric instabilities, which are predecessors to fully developed MLEs that drive stratification through lateral slumping (Thomas et al. 2008; Boccaletti et al. 2007). The signal of high $W_{\mathrm{NT}}$ is patchy and fills the western subtropical NA. Here, values of $R_{N2}$ are large in the west and decrease eastward, consistent with patterns of $Q_{\mathrm{MLE}}$.

In the Southern Hemisphere, elevated $W_{\mathrm{NT}}$ extends east off the southern tip of Africa and continues through the subtropical gyre to the west coast of Australia. This pattern also exists in the South Pacific as wedges extending eastward off the coast of Australia and another extending westward off the archipelagos of southern Chile.

### b. High latitudes

The $Q_{\mathrm{MLE}}$ at the high latitude tends to be a result of deep MLs and modest gradients. Note that $Q_{\mathrm{MLE}}$

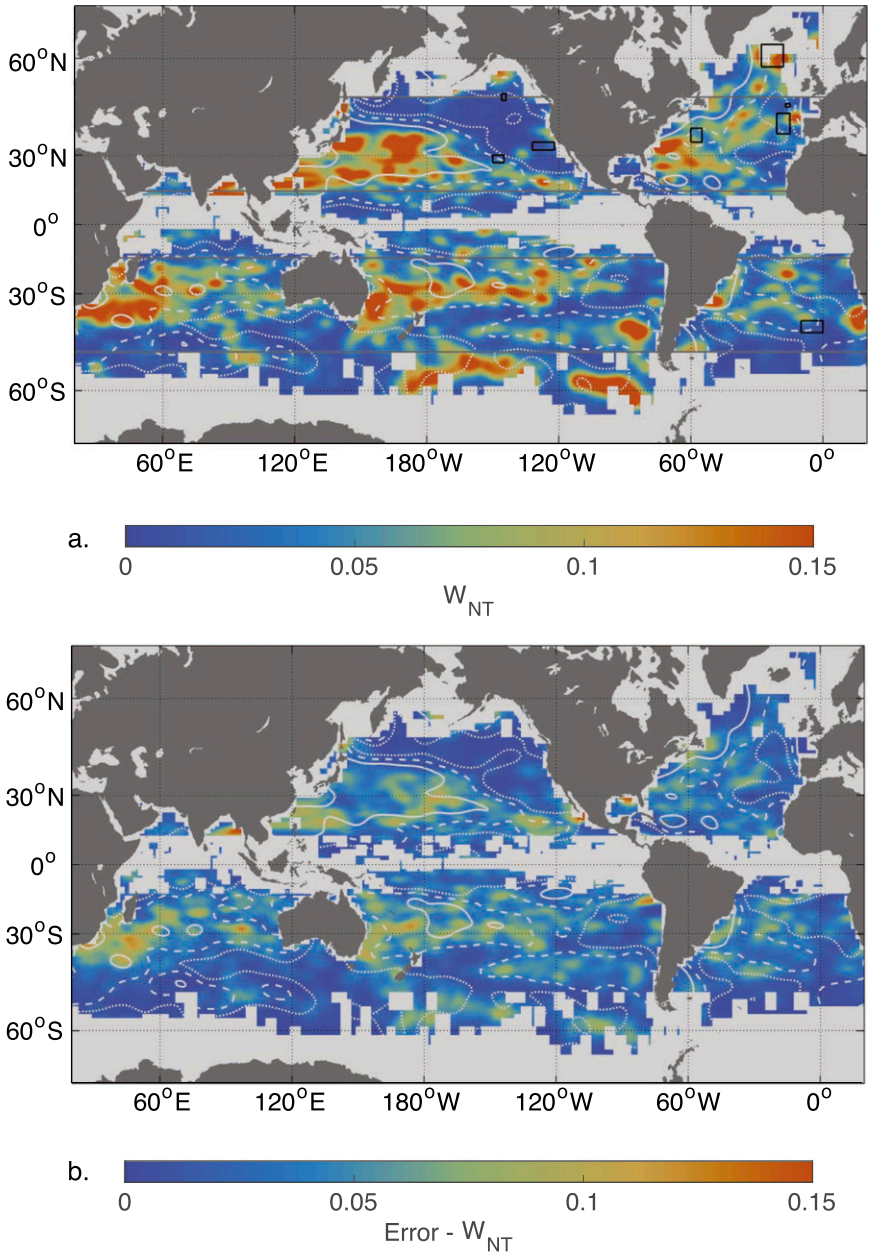


FIG. 6. Metric $W_{NT}$ = Weighted ΔTu × Weighted $R_{N2}$ [(12)]. Higher values of $W_{NT}$ are stronger signatures of increased $R_{N2}$ and smaller values of ΔTu, both of which indicate lateral slumping-induced stratification. Contours of $Q_{MLE}$ at 65 (solid), 35 (dashed), and 20 W m$^{-2}$ (dotted). Black boxes refer to the following observational studies: OWS Papa (150°N, 145°W), Spice (25°N, 140°W; Ferrari and Rudnick 2000), Scalable Lateral Mixing and Coherent Turbulence (LatMix; 37°N, 65°W; Shcherbina et al. 2013), North Pacific Subtropical Front (30°N, 150°W; Hosegood et al. 2006), 2008 North Atlantic Bloom Experiment (NAB08; 60°N, 20°W; Mahadevan et al. 2012), Ocean Surface Mixing, Ocean Sub-mesoscale Interaction Study (OSMOSIS; 48°N, 16°W), Program Océan Multidisciplinaire Méso Echelle (POMME; 42°N, 18°W; Karleskind et al. 2011), and Southern Ocean Seasonal Cycle Experiment (SOSCEX) (10°N, 42°S; Swart et al. 2015). (b) Error in $W_{NT}$.

estimates are not largest in regions of the deepest MLs associated with the ACC and NA (Figs. 5a–c), largely because these regions have weak lateral density gradients. Instead, $Q_{MLE}$ appears in the transition away from the deepest MLs, where MLs, deeper than those found in subtropical fronts, and lateral buoyancy gradients can coexist. The $Q_{MLE}$ associated with these deep MLs agrees with $W_{NT}$ in the subpolar NA, where gradients

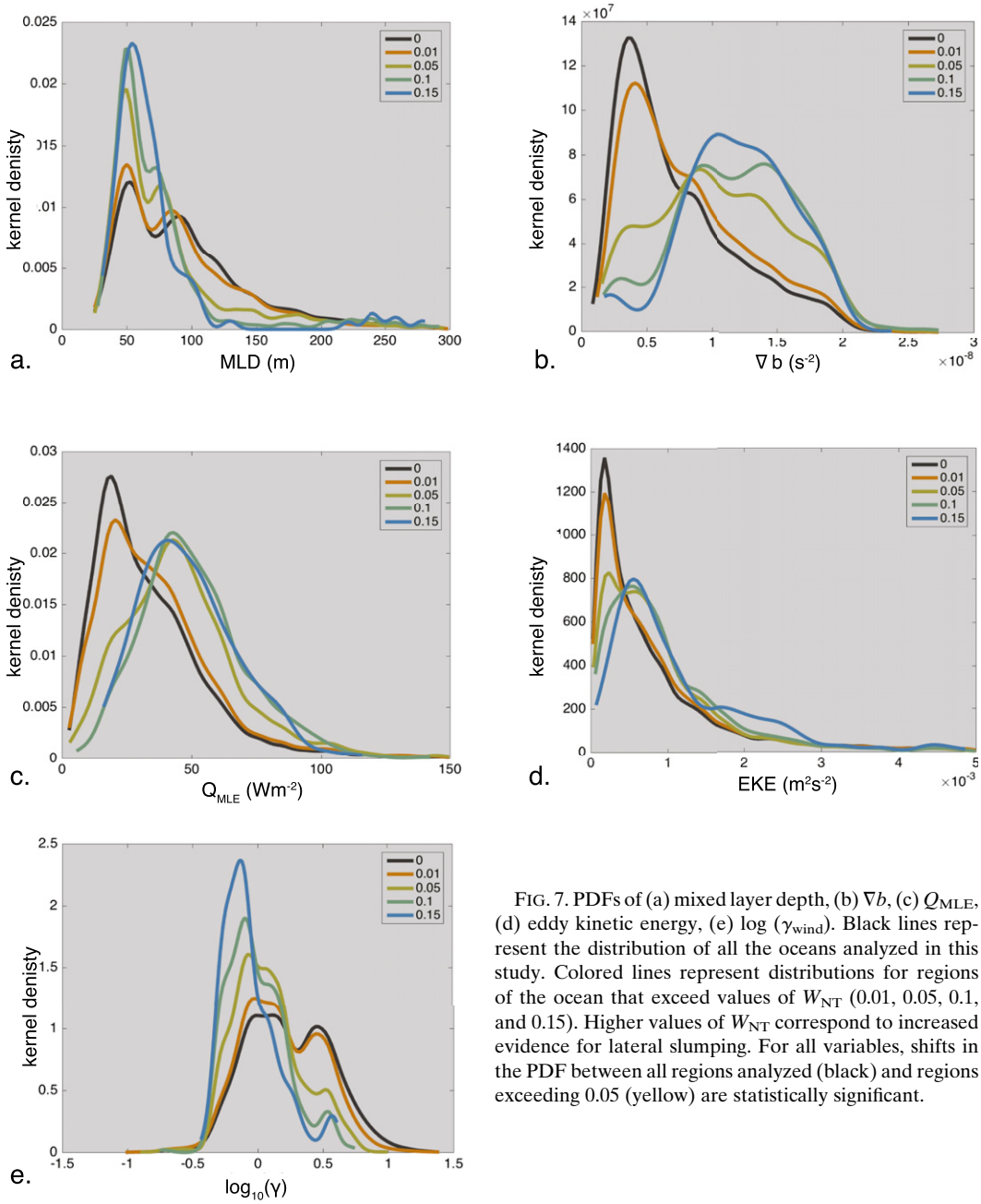


FIG. 7. PDFs of (a) mixed layer depth, (b) $\nabla b$, (c) $Q_{\mathrm{MLE}}$, (d) eddy kinetic energy, (e) log ($\gamma_{\mathrm{wind}}$). Black lines represent the distribution of all the oceans analyzed in this study. Colored lines represent distributions for regions of the ocean that exceed values of $W_{\mathrm{NT}}$ (0.01, 0.05, 0.1, and 0.15). Higher values of $W_{\mathrm{NT}}$ correspond to increased evidence for lateral slumping. For all variables, shifts in the PDF between all regions analyzed (black) and regions exceeding 0.05 (yellow) are statistically significant.

extend from the tip of Newfoundland toward Iceland but disagrees south of Greenland where ΔTu values are large. The $W_{\mathrm{NT}}$ signal in the IB is consistent with the case study (Figs. 2b,d) and with results reported by Mahadevan et al. (2012).

In the Southern Hemisphere, large $Q_{\mathrm{MLE}}$ associated with deep MLs suggests springtime stratification driven by MLEs, conflicting with $W_{\mathrm{NT}}$ patterns that do not show the expected relationship between vertical and lateral TS structure. The existence of high $Q_{\mathrm{MLE}}$ in the southern Indian Ocean around 50°S does not agree with low values of $W_{\mathrm{NT}}$ that result from the large ΔTu. In the South Pacific, the story is the opposite, with high $W_{\mathrm{NT}}$ accompanied by low $Q_{\mathrm{MLE}}$ in a region that extends east from the New Zealand coast toward the southern tip of Chile.

### c. *Equatorial*

The correlation between $W_{\mathrm{NT}}$ and $Q_{\mathrm{MLE}}$ falls off near the equator (Fig. 8) as patchy signals of high $W_{\mathrm{NT}}$ rarely

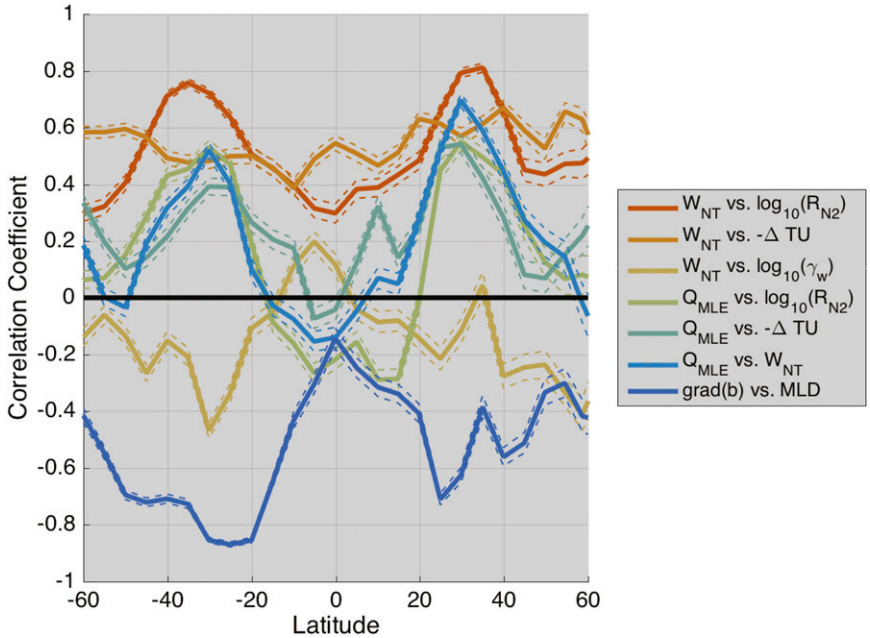


FIG. 8. Latitudinal relationships between $W_{\mathrm{NT}}$ with $R_{N2}$, ΔTu, $\gamma_{\mathrm{wind}}$, and $Q_{\mathrm{MLE}}$; $Q_{\mathrm{MLE}}$ with $R_{N2}$ and ΔTu; and $\nabla b$ with MLD. Positive (negative) values suggest that the two variables are correlated (anticorrelated) within that latitude bin. Here, correlation coefficients between variables were computed in zonal sections of 5° latitude bins. Dotted lines represent 95% confidence intervals.

coexist with regions of high $Q_{\mathrm{MLE}}$ below 20° latitude. There is no strong signal between $W_{\mathrm{NT}}$ and $Q_{\mathrm{MLE}}$ in the Arabian Sea or the Bay of Bengal, which may be attributed to monsoonal dynamics and freshwater fluxes that may dominate the lateral processes here. Fox-Kemper et al. (2008) discuss the implications of $\Psi$ at low latitudes, where the tendency for rapid restratification is accompanied by an increase in eddy growth rates. Near the equator, Rossby adjustment occurs faster and may be important for lateral slumping (Tandon and Garrett 1994). Additionally, the lack of signal in the equatorial regions may reflect uncertainties associated with defining $t_{_\mathrm{QNET0}}$ in tropical regions that exhibit weak or nonexistent seasonal cycles in $Q_{\mathrm{NET}}$.

## 6. Alternative hypotheses

Lateral slumping is ubiquitous where fronts are present, and MLEs may be a leading-order mechanism that slumps fronts, but other lateral processes also modify upper-ocean stratification.

### a. Wind dynamics

Winds interacting with fronts can induce ageostrophic secondary circulations that interact with the effects of MLEs. Winds blowing up/downfront have restratifying/destratifying effects on the upper ocean (Thomas and Lee 2005; Mahadevan et al. 2010) and can sharpen fronts to trigger symmetric instabilities that impact stratification (Taylor and Ferrari 2010; D'Asaro et al. 2011).

Thomas and Ferrari (2008) assess the relative importance of boundary layer dynamics on upper-ocean stratification by deriving estimates for the differential advection in the ML resulting from frontal processes versus frictional processes due to wind stress and geostrophic stress. Studies that estimate the global importance of geostrophic stress (Wenegrat and McPhaden 2016) indicate this process may be influential at low latitudes. Here, the discussion focuses on wind stress where the ratio for differential advection $\Delta v$ is

$$\gamma_{\mathrm{wind}} = \frac{\Delta v_{\mathrm{wind}}}{\Delta v_{\mathrm{front}}} = \frac{(\tau/\rho)^{1/2}\mathrm{Ro}^{-1}}{\nabla b H f^{-1}}, \tag{13}$$

where Ro is the Rossby number, taken here as Ro = 0.1 following Thomas and Ferrari (2008). The term $\gamma_{\mathrm{wind}}$ is computed following the methods used to compute $Q_{\mathrm{MLE}}$ (section 4a), with wind data from CCMP and $\rho$ and $\nabla b$ from MIMOC (Fig. 10a). Positive values imply wind to be dominant, and negative values imply frontogenetic effects to be dominant. It is evident that winds have an influence on upper-ocean stratification where $Q_{\mathrm{MLE}}$ is weak. The magnitude of this scaling depends on the choice of Ro. At the submesoscale, Ro approaches $O(1)$,

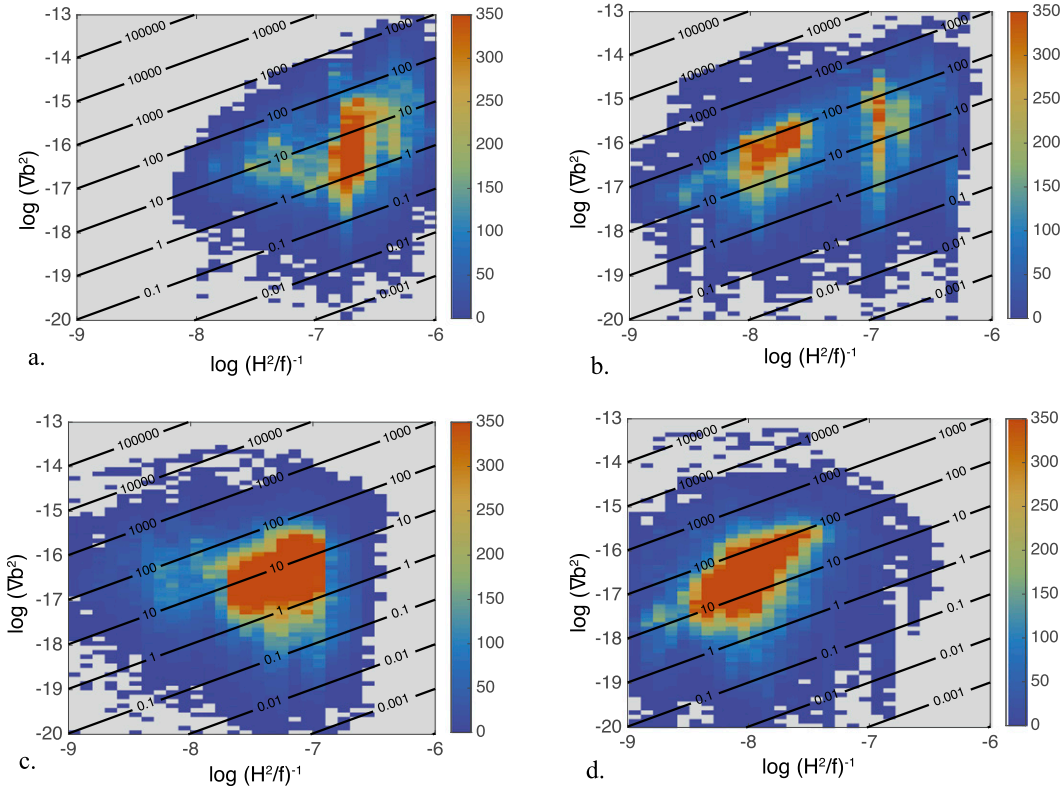


FIG. 9. Probability density function relating surface density gradients $\nabla b$ and mixed layer depths $H$. Contours are $Q_{\mathrm{MLE}} \propto (\nabla b^2 H^2)/f$ [(3)]. (a) Northern Hemisphere (>10°N) summer (August), (b) Northern Hemisphere (>10°N) late winter (February), (c) Southern Hemisphere (>10°S) summer (February), and (d) Southern Hemisphere (>10°S) late winter (August). The summertime relationship between $\nabla b$ and $H$ suggest MLEs do not have a dominant role in setting upper-ocean stratification. Wintertime $H$ increases but appears to be restrained by $\nabla b$. This restraint is shown as most regions of the world's oceans lie on a $Q_{\mathrm{MLE}}$ contour $O(100)$ W m$^{-2}$, consistent with the significance of MLEs on the upper ocean.

decreasing $\gamma_{\mathrm{wind}}$ by an order of magnitude and therefore decreasing the number of regions where wind effects are dominant. Nonetheless, the geographic distribution of $\gamma_{\mathrm{wind}}$ would remain the same and some conclusions may be drawn from these patterns. Correlations between $\log(\gamma_{\mathrm{wind}})$ and $W_{\mathrm{NT}}$ are opposite that of $Q_{\mathrm{MLE}}$ (Fig. 8) with high negative correlation in the midlatitudes, consistent with where frontogenetic dynamics dominate over wind. Correlation falls at high latitudes and near the equator. The absence of strong positive correlation between $\log(\gamma_{\mathrm{wind}})$ and $W_{\mathrm{NT}}$ suggests that wind effects do not describe patterns of frontally enhanced stratification consistently. Similarly, PDFs of $\log(\gamma_{\mathrm{wind}})$ shift toward lower values for regions of high $W_{\mathrm{NT}}$, consistent with the idea that frontogenetic processes are responsible for observed signatures of frontal slumping.

The competing effects of winds on a front can be described as an Ekman buoyancy flux (EBF; Thomas and Lee 2005; D'Asaro et al. 2011):

$$\mathrm{EBF} = \frac{1}{\rho_o}\frac{\tau \nabla b}{f}. \tag{14}$$

Downfront winds drive Ekman transport that moves waters from the dense (cold) side of fronts over less dense waters on the warm side, producing negative EBF that drives vertical mixing and acts to maintain the front. Upfront winds move light (warm) waters over dense (cold), producing positive EBF that drives frontolysis, slumping the front to create vertical stratification. Stratification resulting from positive EBF will have a signature similar to that driven by MLEs and other processes that adiabatically slump horizontal gradients. Observational and numerical evidence of local wind–front interactions illustrate the impact of EBF on the evolution of fronts (Thomas and Lee 2005; Mahadevan et al. 2010; D'Asaro et al. 2011). Some cases find the buoyancy budget driven by EBF rather than MLEs (Haney et al. 2012; Thomas et al. 2016), illustrating the importance of considering these effects when discussing

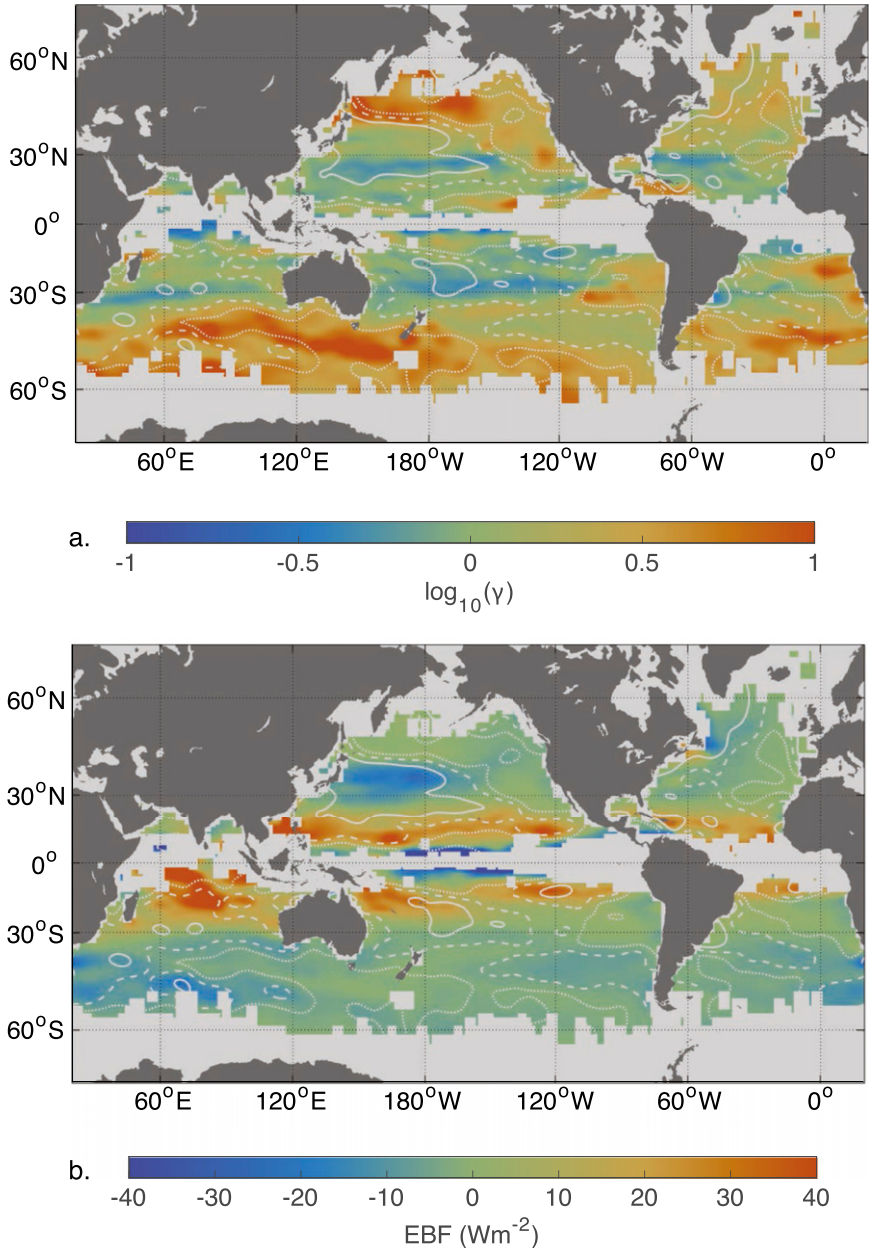


FIG. 10. (a) $\log(\gamma_{\mathrm{wind}})$ negative values suggest that frontal processes dominate upper-ocean stratification, while negative values suggest that wind processes are important. (b) $Q_{\mathrm{EBF}}$ in $\mathrm{W\,m^{-2}}$. Positive values suggest that $Q_{\mathrm{EBF}}$ is stratifying the upper ocean, while negative values indicate winds maintain the front working against MLEs. Contours of $Q_{\mathrm{MLE}}$ at 65 (solid), 35 (dashed), and 20 $\mathrm{W\,m^{-2}}$ (dotted).

global estimates of frontally modulated stratification. EBF can be represented as an equivalent heat flux by multiplying (1) by $[(c_p\rho)/(g\alpha_T)]$ to obtain $Q_{\mathrm{EBF}}$. It is assumed that the effects of EBF and MLE are linear; therefore, $Q_{\mathrm{MLE}}$ and $Q_{\mathrm{EBF}}$ are comparable. Here, wind data from CCMP, and $\rho$ and $\nabla b$ from MIMOC, are processed similar to $Q_{\mathrm{MLE}}$, as described in section 2c, yielding a global distribution of climatological $Q_{\mathrm{EBF}}$ during the transition into spring (Fig. 10b). This climatological view of $Q_{\mathrm{EBF}}$ reveals strong destratifying effects of the westerlies on the Kuroshio (D'Asaro et al. 2011), Gulf Stream (Thomas et al. 2016), and Antarctic polar front and strong restratifying effects in the presence of trade winds.

High-latitude regions lack $W_{\mathrm{NT}}$ (Fig. 6), even in the presence of high $Q_{\mathrm{MLE}}$ (Fig. 5a), evident in the falloff in

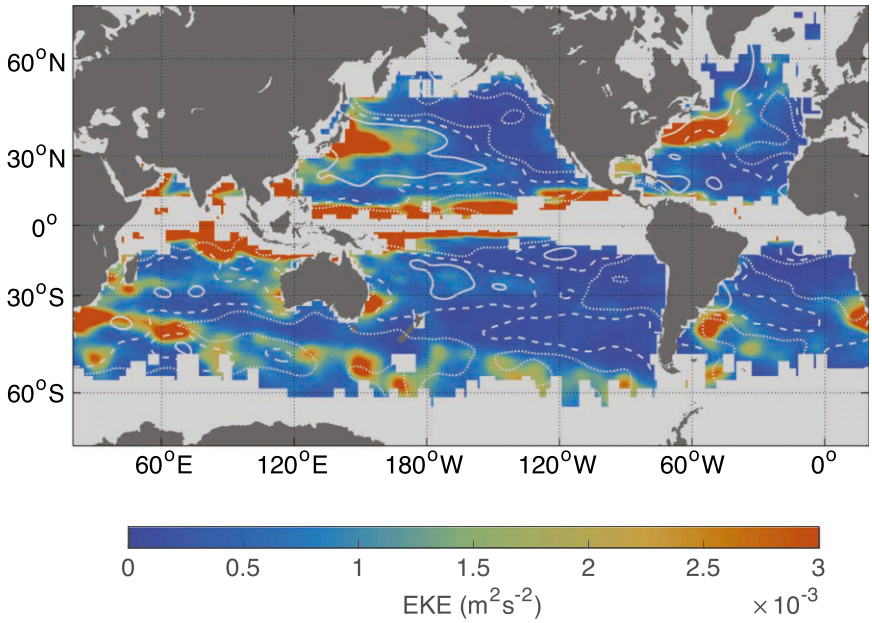


FIG. 11. EKE ($m^2 s^{-2}$) derived from AVISO geostrophic velocity anomalies. Contours of $Q_{MLE}$ at 65 (solid), 35 (dashed), and 20 W $m^{-2}$ (dotted).

correlation between $Q_{MLE}$ and $W_{NT}$ (Fig. 8). This discrepancy occurs in the presence of both negative $Q_{EBF}$ (Fig. 10b) and $\gamma_{wind} > 1$ (Fig. 10a), implying that wind dynamics dominate over frontal effects in setting upper-ocean stratification in these regions. This comparison must be taken with the caveat that large-scale monthly climatologies of winds and density gradients likely misrepresent the impact of EBF on localized fronts, as the instantaneous orientation of winds and fronts will differ from those derived from averages taken over larger spatial and temporal spans. Furthermore, an asymmetry of downfront versus upfront winds implies these values cannot be represented by climatological forcing. Thus, the data and analysis tools employed here may be insufficient to accurately assess the localized role of EBF.

### b. Mesoscale dynamics

Eddy kinetic energy (EKE = $u^2 + v^2$) is calculated from AVISO geostrophic velocity anomalies (http://www.aviso.altimetry.fr/duacs/) and binned as described in section 2. Patterns of high EKE (Fig. 11) coincide with high $Q_{MLE}$ and high $W_{NT}$, particularly near western boundary currents and some sections of the ACC. EKE quiescent regions of the North Pacific, subtropical South Pacific, and the south Indian Ocean south of Australia also coincide with low values of $W_{NT}$. The PDF shift of EKE (Fig. 7) also reflects the concurrence of high $W_{NT}$ and EKE. This might be expected, as submesoscale flows and fronts can emerge from straining and stirring of the mesoscale. Yet, while mesoscale activity can transport buoyancy laterally, the majority of restratification is achieved through vertical transfer of buoyancy resulting from the overturning circulation induced by submesoscale instabilities (Fox-Kemper et al. 2008).

### c. Unresolved processes

Other causes may be responsible for the discrepancy between observed and modeled stratification during the transition into spring. Here, the discussion of the Turner angle is extended to include modeled Turner angle $Tu_M$, calculated using model output similar to $Tu_V$ [(7)], and $\Delta Tu_{OM} = |Tu_M - Tu_V|$, similar to $\Delta Tu$ (section 3c). The angles $\Delta Tu_{OM}$ and $\Delta Tu$ are used to partition the ocean into five categories (Fig. 12). While diagnosing all possible dynamics is beyond the scope of this analysis, some general conclusions can be inferred from this representation. Category A contains regions consistent with vertical mixing (e.g., I and II in Fig. 1). These account for 24% of the oceans analyzed and are most prominent in the subpolar North Pacific. Category B consists of regions consistent with lateral slumping (e.g., IV in Fig. 1) and account for 14% of oceans analyzed in this study. Category C includes regions where observations agree with both vertical mixing and lateral slumping and accounts for 27% of the oceans analyzed. Note that category C characterizes regions within the subtropics, where horizontal density gradients are strong, $Q_{MLE}$ is high, and $Q_{EBF}$ is positive. Category D is made up of regions where observations do not agree with vertical mixing or frontal slumping. This accounts for 13% of the

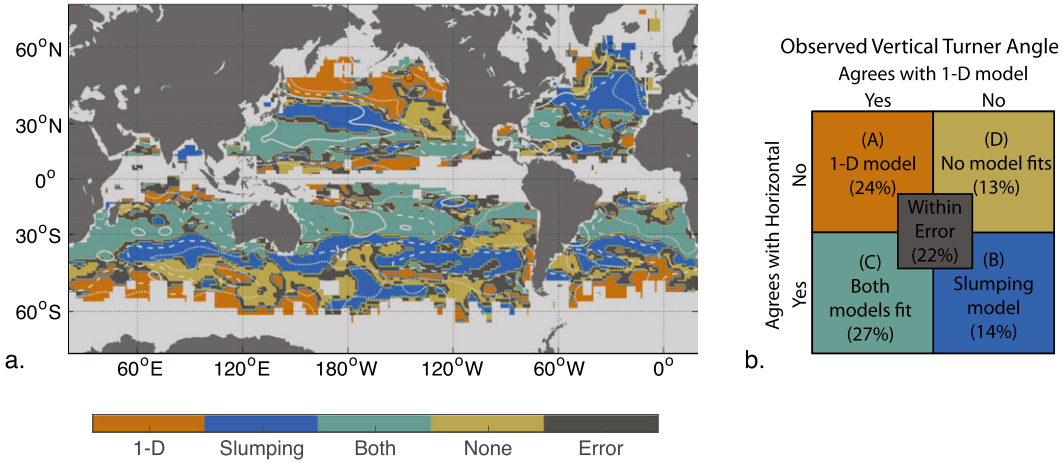


FIG. 12. (a) Observed Turner angle is compared with modeled vertical and horizontal Turner angles (see Fig. 1). Contours of $Q_{\mathrm{MLE}}$ at 65 (solid), 35 (dashed), and 20 W m$^{-2}$ (dotted). (b) Descriptions of each of these categories are summarized, where agreement is set at a threshold of $\Delta\mathrm{Tu} < 30$. $\Delta\mathrm{Tu}_{\mathrm{OM}} < 30$ (Quadrant A), $\Delta\mathrm{Tu} < 30$ (Quadrant B), both $\Delta\mathrm{Tu}_{\mathrm{OM}} < 30$ and $\Delta\mathrm{Tu} < 30$ (Quadrant C), and both $\Delta\mathrm{Tu}_{\mathrm{OM}} > 30$ and $\Delta\mathrm{Tu} > 30$ (Quadrant D).

regions analyzed and may point to the importance of other lateral processes. For example, category D characterizes regions of the ACC. While MLEs are thought to be leading order on time scales shorter than most large-scale geostrophic flows, this may not be true for some of the fastest currents. The final category consists of regions where differences in Turner angle are within error of these different categories and account for 22% of the ocean analyzed.

## 7. Conclusions

Profiling float observations compared to a one-dimensional model of the ocean ML suggest that parameterizations ignoring lateral processes underestimate upper-ocean springtime stratification for 75% ± 25% of the world's oceans. Relationships between the large-scale horizontal TS and local vertical TS are used to identify regions where lateral gradients are transformed into vertical stratification. This analysis indicates that lateral slumping is most likely responsible for 40% ± 25% of the increased stratification not captured by the models, therefore influencing 30% ± 20% of the world's oceans. Patterns of lateral slumping (larger $W_{\mathrm{NT}}$) mimic patterns of parameterized MLE (high $Q_{\mathrm{MLE}}$), with 60% ± 10% of regions with $W_{\mathrm{NT}} > 0.05$ having an associated $Q_{\mathrm{MLE}}$ flux $> 40\,\mathrm{W\,m^{-2}}$ (Fig. 2c). This correspondence suggests that MLEs have an important role in stratifying the upper ocean during the transition into spring. Specifically, regions of high $W_{\mathrm{NT}}$ tend to have strong lateral density gradients and moderate mixed layer depths, with a small distribution of $W_{\mathrm{NT}}$ in high-latitude regions of the NA and Southern Ocean with deep MLs.

Fox-Kemper et al. (2011) parameterized MLEs into global circulation models using (1) with $\Psi = (\Delta s/L_f)\Psi_o$. Including this parameterization shallows the MLD in the North Pacific extending east of Japan, in the Gulf of Mexico, in basins extending both east and west from Australia, and in the Southern Ocean, which are all consistent with patterns of $W_{\mathrm{NT}}$ found here. However, patterns of high $W_{\mathrm{NT}}$ in the shallow ML regions of the subtropics found here are not in agreement with Fox-Kemper et al. (2011); this may reveal limitations of (1) to capture MLEs in shallow MLs or may be attributed to the importance of other stratifying processes in the subtropics.

Despite evidence from observations and models that indicate the importance of wind stress on frontal stratification via the Ekman buoyancy flux, the large-scale patterns of $Q_{\mathrm{EBF}}$ calculated here do not further improve the predictions of $W_{\mathrm{NT}}$. This is most likely due to the inability of large-scale wind and gradient statistics to capture local dynamics. This study suggests the relative contributions of EBF to large-scale patterns of upper-ocean stratification are not resolved by this analysis.

Although this study focuses on springtime stratification, the relationship between $H$ and $\nabla b$ (Fig. 8) indicates that MLEs could limit the depth of the wintertime ML in regions with strong lateral gradients, with a typical restratification flux of $O(100)\,\mathrm{W\,m^{-2}}$. This is consistent with studies showing heightened submesoscale activity in winter (Callies et al. 2015). Analogous to spring stratification, MLEs could also influence stratification during fall as surface forcing works to deepen mixed layers in the presence of strong summer lateral density gradients. The full seasonal implications of lateral slumping remain to be explored.

*Acknowledgments.* We thank Baylor Fox-Kemper and one anonymous reviewer, whose careful and insightful suggestions improved this manuscript. This work was supported by Office of Naval Research Grants N00014-09-1-0266 and N00014-10-1-0311 (LJ and CML) and N00014-09-1-0172 and National Science Foundation Grant OCE0934580 (EAD). Argo data were collected and made available freely by the International Argo program and the national programs that contribute to it (http://www.argo.ucsd.edu). The Argo program is part of the Global Ocean Observing System. NCEP reanalysis data were obtained through the NCAR Computational and Information Systems Lab Research Data Archive website (http://rda.ucar.edu/). MIMOC was provided by NOAA (http://www.pmel.noaa.gov/mimoc/).

## REFERENCES

Belcher, S. E., and Coauthors, 2012: A global perspective on Langmuir turbulence in the ocean surface boundary layer. *Geophys. Res. Lett.*, **39**, L18605, doi:10.1029/2012GL052932.

Boccaletti, G., R. Ferrari, and B. Fox-Kemper, 2007: Mixed layer instabilities and restratification. *J. Phys. Oceanogr.*, **37**, 2228–2250, doi:10.1175/JPO3101.1.

Callies, J., R. Ferrari, J. Klymak, and J. Gula, 2015: Seasonality in submesoscale turbulence. *Nat. Commun.*, **6**, 6862, doi:10.1038/ncomms7862.

Capet, X., J. C. McWilliams, M. J. Molemaker, and A. F. Shchepetkin, 2008: Mesoscale to submesoscale transition in the California Current System. Part I: Flow structure, eddy flux, and observational tests. *J. Phys. Oceanogr.*, **38**, 29–43, doi:10.1175/2007JPO3671.1.

Danabasoglu, G., S. C. Bates, B. P. Briegleb, S. R. Jayne, M. Jochum, W. G. Large, S. Peacock, and S. G. Yeager, 2012: The CCSM4 ocean component. *J. Climate*, **25**, 1361–1389, doi:10.1175/JCLI-D-11-00091.1.

D'Asaro, E., C. Lee, L. Rainville, R. Harcourt, and L. Thomas, 2011: Enhanced turbulence and energy dissipation at ocean fronts. *Science*, **332**, 318–322, doi:10.1126/science.1201515.

Dunne, J. P., and Coauthors, 2012: GFDL's ESM2 global coupled climate-carbon Earth System Models. Part I: Physical formulation and baseline simulation characteristics. *J. Climate*, **25**, 6646–6665, doi:10.1175/JCLI-D-11-00560.1.

Emerson, S., and C. Stump, 2010: Net biological oxygen production in the ocean—II: Remote in situ measurements of $O_2$ and $N_2$ in subarctic Pacific surface waters. *Deep-Sea Res. II*, **57**, 1255–1265, doi:10.1016/j.dsr.2010.06.001.

Ferrari, R., and D. L. Rudnick, 2000: Thermohaline variability in the upper ocean. *J. Geophys. Res.*, **105**, 16 857–16 883, doi:10.1029/2000JC900057.

Fox-Kemper, B., and R. Ferrari, 2008: Parameterization of mixed layer eddies. Part II: Prognosis and impact. *J. Phys. Oceanogr.*, **38**, 1166–1179, doi:10.1175/2007JPO3788.1.

——, ——, and R. Hallberg, 2008: Parameterization of mixed layer eddies. Part I: Theory and diagnosis. *J. Phys. Oceanogr.*, **38**, 1145–1165, doi:10.1175/2007JPO3792.1.

——, and Coauthors, 2011: Parameterization of mixed layer eddies. III: Implementation and impact in global ocean climate simulations. *Ocean Modell.*, **39**, 61–78, doi:10.1016/j.ocemod.2010.09.002.

Gill, A. E., and P. P. Niller, 1973: The theory of the seasonal variability in the ocean. *Deep-Sea Res. Oceanogr. Abstr.*, **20**, 141–177, doi:10.1016/0011-7471(73)90049-1.

Haney, S., and Coauthors, 2012: Hurricane wake restratification rates of one-, two- and three-dimensional processes. *J. Mar. Res.*, **70**, 824–850, doi:10.1357/002224012806770937.

Hosegood, P., M. C. Gregg, and M. H. Alford, 2006: Sub-mesoscale lateral density structure in the oceanic surface mixed layer. *Geophys. Res. Lett.*, **33**, L22604, doi:10.1029/2006GL026797.

——, ——, and ——, 2013: Wind-driven submesoscale subduction at the North Pacific subtropical front. *J. Geophys. Res. Oceans*, **118**, 5333–5352, doi:10.1002/jgrc.20385.

Hoskins, B. J., and F. P. Bretherton, 1972: Atmospheric frontogenesis models: Mathematical formulation and solution. *J. Atmos. Sci.*, **29**, 11–37, doi:10.1175/1520-0469(1972)029<0011:AFMMFA>2.0.CO;2.

IOC, SCOR, and IAPSO, 2010: The International Thermodynamic Equation of Seawater—2010: Calculation and use of thermodynamic properties. Intergovernmental Oceanographic Commission, Manuals and Guides 56, 220 pp. [Available online at http://www.teos-10.org/pubs/TEOS-10_Manual.pdf.]

Johnson, G. C., S. Schmidtko, and J. M. Lyman, 2012: Relative contributions of temperature and salinity to seasonal mixed layer density changes and horizontal density gradients. *J. Geophys. Res.*, **117**, C04015, doi:10.1029/2011JC007651.

Karleskind, P., M. Lévy, and L. Mémery, 2011: Modifications of mode water properties by sub-mesoscales in a bio-physical model of the northeast Atlantic. *Ocean Modell.*, **39**, 47–60, doi:10.1016/j.ocemod.2010.12.003.

Kraus, E. B., and J. S. Turner, 1967: A one-dimensional model of the seasonal thermocline II. The general theory and its consequences. *Tellus*, **19A**, 98–106, doi:10.1111/j.2153-3490.1967.tb01462.x.

Large, W. G., J. C. McWilliams, and S. C. Doney, 1994: Oceanic vertical mixing: A review and a model with a nonlocal boundary layer parameterization. *Rev. Geophys.*, **32**, 363–403, doi:10.1029/94RG01872.

Mahadevan, A., A. Tandon, and R. Ferrari, 2010: Rapid changes in mixed layer stratification driven by submesoscale instabilities and winds. *J. Geophys. Res.*, **115**, C03017, doi:10.1029/2008JC005203.

——, E. D'Asaro, C. Lee, and M. J. Perry, 2012: Eddy-driven stratification initiates North Atlantic spring phytoplankton blooms. *Science*, **337**, 54–58, doi:10.1126/science.1218740.

Price, J. F., R. A. Weller, and R. Pinkel, 1986: Diurnal cycling: Observations and models of the upper ocean response to diurnal heating, cooling, and wind mixing. *J. Geophys. Res.*, **91**, 8411–8427, doi:10.1029/JC091iC07p08411.

Roemmich, D., and Coauthors, 2009: The Argo Program: Observing the global ocean with profiling floats. *Oceanography*, **22**, 34–43, doi:10.5670/oceanog.2009.36.

Schmidtko, S., G. C. Johnson, and J. M. Lyman, 2012: Monthly Isopycnal/Mixed-layer Ocean Climatology (MIMOC). NOAA, accessed 9 February 2013. [Available online at http://www.pmel.noaa.gov/mimoc.]

Shcherbina, A. Y., M. C. Gregg, M. H. Alford, and R. R. Harcourt, 2009: Characterizing thermohaline intrusions in the North Pacific subtropical frontal zone. *J. Phys. Oceanogr.*, **39**, 2735–2756, doi:10.1175/2009JPO4190.1.

——, E. A. D'Asaro, C. M. Lee, J. M. Klymak, M. J. Molemaker, and J. C. McWilliams, 2013: Statistics of vertical vorticity, divergence, and strain in a developed submesoscale turbulence field. *Geophys. Res. Lett.*, **40**, 4706–4711, doi:10.1002/grl.50919.

Sutherland, G., G. Reverdin, L. Marié, and B. Ward, 2014: Mixed and mixing layer depths in the ocean surface boundary layer under conditions of diurnal stratification. *Geophys. Res. Lett.*, **41**, 8469–8476, doi:10.1002/2014GL061939.

Sverdrup, H., 1953: On conditions for the vernal blooming of phytoplankton. *J. Cons. Int. Explor. Mer*, **18**, 287–295, doi:10.1093/icesjms/18.3.287.

Swart, S., S. J. Thomalla, and P. M. S. Monteiro, 2015: The seasonal cycle of mixed layer dynamics and phytoplankton biomass in the Sub-Antarctic Zone: A high-resolution glider experiment. *J. Mar. Syst.*, **147**, 103–115, doi:10.1016/j.jmarsys.2014.06.002.

Tandon, A., and C. Garrett, 1994: Mixed layer restratification due to a horizontal density gradient. *J. Phys. Oceanogr.*, **24**, 1419–1424, doi:10.1175/1520-0485(1994)024<1419:MLRDTA>2.0.CO;2.

Taylor, J. R., and R. Ferrari, 2010: Buoyancy and wind-driven convection at mixed layer density fronts. *J. Phys. Oceanogr.*, **40**, 1222–1242, doi:10.1175/2010JPO4365.1.

Thomas, L. N., and C. M. Lee, 2005: Intensification of ocean fronts by down-front winds. *J. Phys. Oceanogr.*, **35**, 1086–1102, doi:10.1175/JPO2737.1.

——, and R. Ferrari, 2008: Friction, frontogenesis, and the stratification of the surface mixed layer. *J. Phys. Oceanogr.*, **38**, 2501–2518, doi:10.1175/2008JPO3797.1.

——, A. Tandon, and A. Mahadevan, 2008: Submesoscale processes and dynamics. *Ocean Modeling in an Eddying Regime*, *Geophys. Monogr.*, Vol. 177, 17–38, doi:10.1029/177GM04.

——, J. R. Taylor, E. A. D'Asaro, C. M. Lee, J. M. Klymak, and A. Shcherbina, 2016: Symmetric instability, inertial oscillations, and turbulence at the Gulf Stream front. *J. Phys. Oceanogr.*, **46**, 197–217, doi:10.1175/JPO-D-15-0008.1.

Wenegrat, J. O., and M. J. McPhaden, 2016: Wind, waves, and fronts: Frictional effects in a generalized Ekman model. *J. Phys. Oceanogr.*, **46**, 371–394, doi:10.1175/JPO-D-15-0162.1.

Worthington, L. V., 1953: The 18° water in the Sargasso Sea. *Deep-Sea Res.*, **5**, 297–305, doi:10.1016/0146-6313(58)90026-1.